

Per-separation clustered-dot color halftone watermarks: separation estimation based on spatial frequency content

Basak Oztan*

University of Rochester
Department of Electrical and Computer Engineering
Rochester, New York 14627-0126

Gaurav Sharma

University of Rochester
Department of Electrical and Computer Engineering
and
Department of Biostatistics and Computational Biology
Rochester, New York 14627-0126
E-mail: gaurav.sharma@rochester.edu

Abstract. A framework for clustered-dot color halftone watermarking is considered, wherein watermark patterns are embedded in individual colorant halftones prior to printing and embedded watermarks are detected from scans of the printed images after obtaining estimates of the individual halftone separations. The principal challenge in this methodology arises in the watermark detection phase. Typical three-channel RGB scanner systems do not directly provide good estimates of the four CMYK colorant halftones that are commonly used in color printing systems. To address this challenge, we propose an estimation method that, when used with suitably selected halftone periodicities, jointly exploits the differences in the spatial periodicities and the color (spectra) of the halftone separations to obtain good estimates of the individual halftones from conventional RGB scans. We demonstrate the efficacy of this methodology experimentally using continuous phase modulation for the embedding of independent visual watermark patterns in the individual halftone separations. Watermarks detected from the estimates of halftone separations obtained using the proposed estimation method have a much higher contrast than those detected directly. We also evaluate the accuracy of the estimated halftones through simulations and demonstrate that the proposed estimation method offers high accuracy. © 2010 SPIE and IS&T. [DOI: 10.1117/1.3497615]

1 Introduction

Digital watermarks have recently emerged as an important enabling technology for security and forensics applications for multimedia^{3–6} and for hardcopy (Ref. 7, Chap. 5, and Ref. 8). In the hardcopy domain these techniques provide

functionality that mimics or extends the capabilities of conventional paper watermarks that have been extensively utilized since their introduction in the late thirteenth century.⁹

Since most hardcopy reproduction relies on halftone printing, methods that embed the watermark in the halftone structure comprise one of the primary categories of hardcopy digital watermarks. These methods enable printed images to carry watermark data in the form of changes in the halftone structures, which are normally imperceptible but can be distinguished by appropriate detection methods. The proposed methods for detection of halftone watermarks can involve either scanning and digital processing or manual detection, wherein the ordinarily imperceptible watermark pattern is rendered visible by overlaying the printed image with a decoder mask such as a preprinted transparency. Because the manual process can also be simulated in the digital processing, manually detectable watermarks can typically also be detected via digital processing, whereas the converse does not necessarily hold. A number of techniques have been proposed for halftone-based watermarking in black and white, i.e., monochrome, printing systems.^{10–20} Most of these methods, however, do not directly generalize to color. Thus, there is an unmet need for color halftone watermarking techniques. This need is exacerbated by the fact that image content is often printed in color, particularly as color printing systems become more affordable and accessible.

Since the colorant halftone separations are printed sequentially and overlaid on the paper substrate, per-channel embedding and detection of watermark patterns is an attractive option that would extend monochrome watermarking methods to color. To detect the watermark patterns, one would like to acquire the constituent halftone separations used in the color printing system from the (overlaid) print. This would work, for example, if one could deploy a scanner with N color channels, where each color channel captures only one of the N colorants used in the printing system. In actual practice, desktop scanners commonly use RGB color filters to capture color. For three-color CMY printing, as illustrated in

*Currently with the Department of Computer Science, Rensselaer Polytechnic Institute, Troy, New York 12180.

This paper is available online as an open-access article, with color versions of several of the figures. In particular, Figs. 1, 2, 4 and 29 may be difficult to interpret without color; print readers should refer to the online version at <http://SPIEDigitalLibrary.org> for these figures.

Paper 10002PRR received Jan. 5, 2010; revised manuscript received Aug. 11, 2010; accepted for publication Aug. 24, 2010; published online Dec. 16, 2010

1017-9909/2010/19(4)/043007/22/\$25.00 © 2010 SPIE and IS&T.

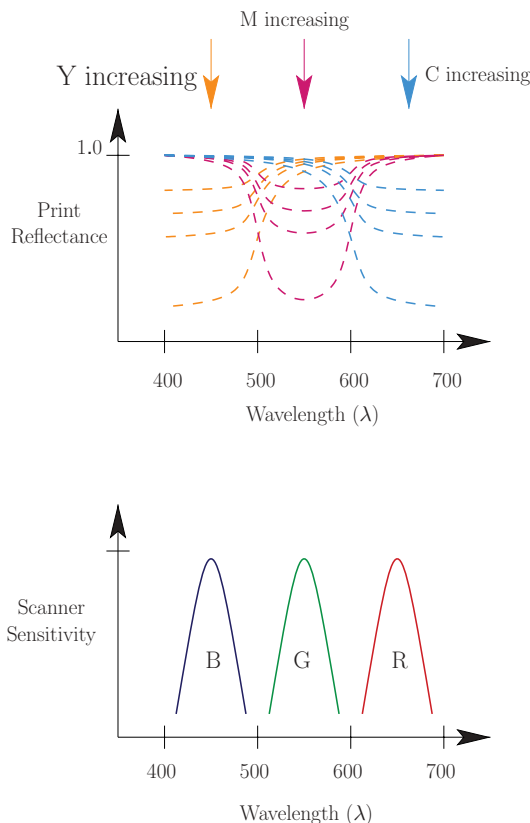


Fig. 1 Complementary relation between printer *CMY* colorants and scanner *RGB* channels. (Color online only.)

Fig. 1, there is a complementary relationship between the *CMY* colorants and *RGB* scanner channels: the cyan (*C*), magenta (*M*), and yellow (*Y*) colorants absorb light, respectively, over the spectral regions in which the red (*R*), green (*G*), and blue (*B*) scanner channels are sensitive. Thus, in an ideal setting, *C*, *M*, and *Y* colorant halftones may be estimated from the scanner *R*, *G*, and *B* channels, respectively. In practice, however, this is usually not feasible for a couple of reasons. First, typical printing systems utilize *CMYK* (four) colorants. The black (*K*) colorant absorbs uniformly across the spectrum, and thus it consistently appears in the scanner *RGB* channels. Second, so-called “unwanted absorptions” of the *CMY* colorants also cause cross-coupling, i.e., *C*, *M*, and *Y* halftone separations not only appear in the scan *R*, *G*, and *B* channels that complement their spectral absorption bands,

respectively, but also in the two other channels as well. The image of Fig. 2 illustrates the couplings between the *CMYK* halftone separations in the scanner *RGB* channels. Due to these undesired couplings, the four *C*, *M*, *Y*, and *K* halftone separations cannot be directly obtained from individual *R*, *G*, and *B* scanner channel responses.

In this paper, we present a methodology for estimating individual *C*, *M*, *Y*, and *K* halftones from *RGB* scans of printed images by jointly exploiting the differences between suitably selected spatial halftone periodicities and the differences in the spectral characteristics of the colorants. We use the proposed joint estimation scheme to extend, to color halftone printing, the halftone watermarking method using continuous phase modulation²¹ (CPM), which embeds and detects a visual watermark pattern. Our experiments demonstrate that the estimated halftones obtained via the proposed method improve the detection of the embedded CPM watermarks, offering much higher contrast for the detected watermark patterns than direct detection. Because the estimation methodology works only with electronic processing, the proposed method is not applicable to direct detection of the watermark in the printed image by physical overlay using a suitable decoder mask.

The framework we present may also be independently viewed as a general method for estimating *CMYK* halftone separations from *RGB* scans. We evaluate the accuracy of the proposed method in this context via simulations and compare against alternatives that use either the difference in spatial periodicities or in spectral characteristics alone (for the estimation of the halftones). Our results demonstrate that the combined methodology offers a significant advantage.

The presented work builds on and extends our prior work in this area¹ that addressed the more limited setting of three-color *CMY* printing and improves on our preliminary report on this effort² by utilizing a suitable model for analysis and processing. Note that our framework relies on data embedding in the individual spatial patterns of the constituent *CMYK* halftones. This is complementary to alternate methods^{22–26} that have previously been proposed for data hiding in printed color images using spectral characteristics alone. Also, dot-on-dot²⁷ color halftone watermarking with the same watermark embedded in each colorant channel can be viewed as an alternative, though rather restrictive, framework for extending monochrome halftone watermarking methods to color.²⁸



Fig. 2 *RGB* scan of a printed image that was divided into four stripes, where the stripes from left to right contain only *C*, *M*, *Y*, and *K* colorants, respectively. The *K* colorant can be consistently observed in all scan channels and cross-coupling between *C*, *M*, and *Y* colorant halftone separations can also be clearly seen in the scan *R*, *G*, and *B* channels. (a) *RGB* scan of *CMYK* halftone; (b) scan *R* channel; (c) scan *G* channel, and (d) scan *B* channel. (Color online only.)

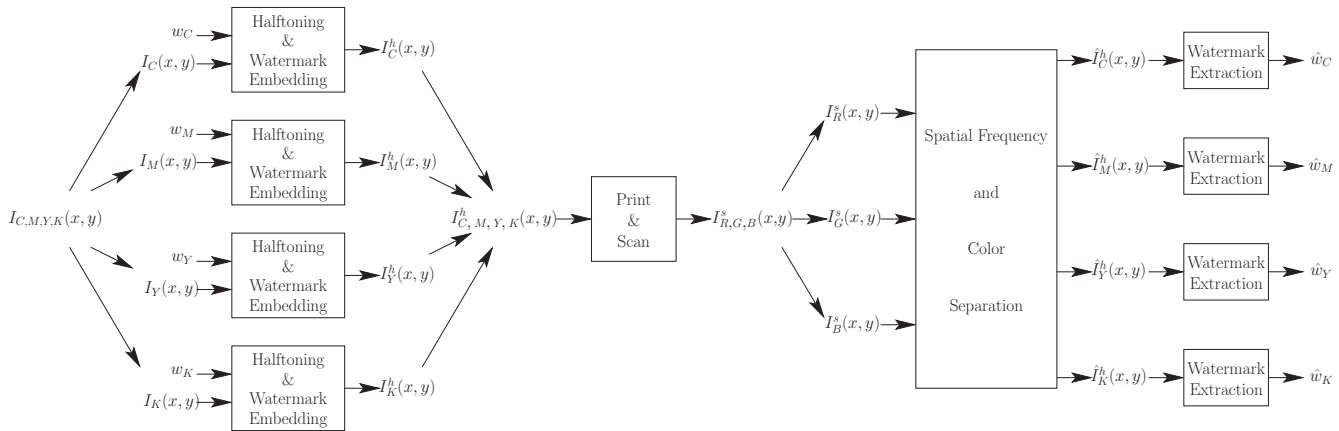


Fig. 3 Overview of per-channel basis clustered-dot color halftone watermarking by exploiting spatial frequency and color separation methodology.

The rest of the paper is organized as follows. Section 2 describes our framework for clustered-dot color halftone watermarking. Section 3 describes our method for estimating *CMYK* halftone separations from *RGB* scans exploiting the differences in spatial frequency and colorant spectra. The watermarking technique used to test our framework is described in Sec. 4, and the experimental results are presented in Sec. 5. Finally, in Sec. 6, we present conclusions.

2 Clustered-Dot Color Halftone Watermarking

For typical *CMYK* printing, the overall watermark embedding and extraction scheme that we consider is illustrated in Fig. 3. The input cover image $I_{C,M,Y,K}(x, y)$ is a contone *CMYK* image that is typically obtained by transforming a device-independent colorimetric representation of the image to the device-dependent *CMYK* values via a set of color conversions.²⁹ The watermark w_i for the i 'th colorant separation $I_i(x, y)$, where i is one of C, M, Y , or K , is embedded in the halftone separation $I_i^h(x, y)$ in the halftoning stage. For the method we demonstrate, the watermark w_i will in fact be a spatial pattern $w_i(x, y)$ corresponding, for instance, to rasterized text or a logo. The color halftone image $I_{C,M,Y,K}^h(x, y)$ is obtained by printing the constituent halftone separations in overlay. For the detection of the watermark patterns embedded in these separations, a scan $I_{R,G,B}^s(x, y)$ of the printed image is obtained using a conventional *RGB* scanner.

To obtain estimates of the four constituent halftone separations from these three channels, additional information is required. Here, we rely on the spatial and spectral characteristics of rotated clustered-dot color halftones²⁷ to provide a solution to this problem. If the halftone frequencies are suitably chosen, the differences in spatial periodicities and colorant spectra can be jointly exploited to obtain estimates of the C, M, Y , and K halftone separations from the R, G , and B channels $I_k^s(x, y)$, $k \in \{R, G, B\}$, of the scanned image—as is described in Sec. 3. Once the estimate $\hat{I}_i^h(x, y)$ is obtained for the i th colorant halftone, the monochrome watermark detection method can be applied to the separation in order to recover (an estimate of) the corresponding watermark w_i .

3 Halftone Separation Estimation Exploiting Differences in Spatial Periodicity and Colorant Spectra

Our goal is to obtain estimates of the *CMYK* halftone separations $\hat{I}_i^h(x, y)$, $i \in \{C, M, Y, K\}$, from the *RGB* channels of the scanned image $I_k^s(x, y)$, $k \in \{R, G, B\}$. The halftones $I_i^h(x, y)$ and their estimates $\hat{I}_i^h(x, y)$, $i \in \{C, M, Y, K\}$, are binary images, where we adopt the convention that the values 1 and 0 correspond, respectively, to whether ink/toner i is, or is not, deposited (or estimated to be deposited) at the pixel position (x, y) . On the other hand, the k th color channel of the scanner $I_k^s(x, y)$ is a contone image, where the image value at pixel position (x, y) represents the fraction of the light reflected from the pixel (x, y) within the transmittance band of the k th scanner channel.

As we pointed out earlier, for typical desktop *RGB* scanners, coupling between the different colorant halftones in the scanned *RGB* image is inevitable. Figures 4(a) to 4(d) show enlarged views of a region from the digital M halftone separation, digital *CMYK* halftone separation overlay, scanned *RGB* image, and scan G channel of an image used in our experiments to test our framework, respectively. It is apparent not only is the halftone structure of the desired M separation visible, but due to the fact that the C, Y , and K separations also have absorption in the scanner G channel, the undesired halftone structure for these separations can be seen in the G channel with varying intensities. This interference can be also observed in the frequency domain. Figure 5 shows enlarged view of the log-magnitude Fourier spectrum of the G channel image for the experimental data around low-frequency regions. The Fourier spectrum exhibits peaks not only about the fundamental frequency vectors (and higher order harmonics) of the M separation, but also at the fundamental frequency vectors of C, Y , and K separations, and moiré frequencies. We exploit the fact that, when suitably designed, these peaks appear at distant locations in the frequency domain and unwanted frequency components can be eliminated by spatial filtering.

A schematic overview of our color halftone separation estimation algorithm is shown in Fig. 6. First, we obtain, via spatial filtering, an estimate of (black) K halftone separation using the scan *RGB* channel images jointly. Detailed

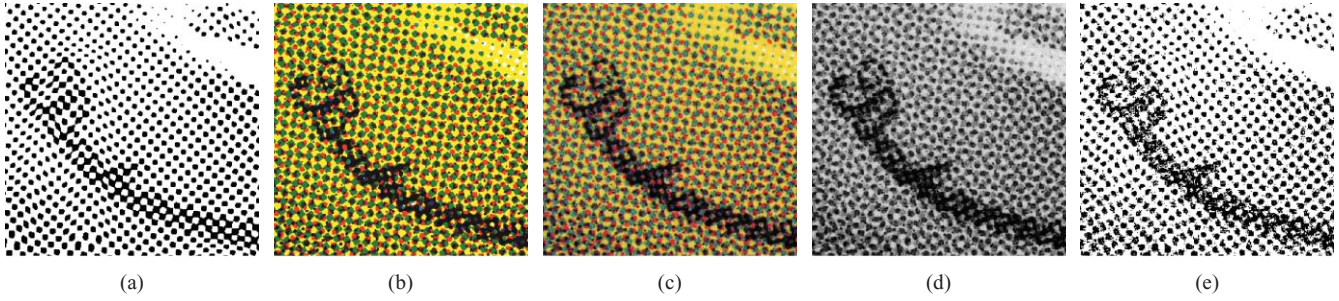


Fig. 4 (a) Enlarged view of a region from the digital M halftone separation of “Hats” halftone image used in our experiments $I_M^h(x, y)$, (b) the same region from the digital $CMYK$ halftone overlay $I_{C,M,Y,K}^h(x, y)$, (c) approximately the same region from the RGB scanned color halftone print $I_{R,G,B}^s(x, y)$, (d) the region from the G channel image of the scanned print showing the couplings between the halftone structures of M and C , Y , and K separations $I_G^s(x, y)$, and (e) the region from the M halftone estimate obtained using our methodology $\hat{I}_M^h(x, y)$. (Color online only.)

description of this process is presented in Sec. 3.2. The estimate of the K halftone separation is then utilized together with each of the scanner R , G , and B channel images to obtain estimates of the complementary C , M , and Y halftone separations, respectively, where once again, the spatial and spectral information is used jointly. The estimation process of CMY halftone separations is described in detail in Sec. 3.3 and a sample estimate obtained from the scanned image of Fig. 4(d) for the magenta separation, for approximately the same regions as Fig. 4(a), is shown in Fig. 4(e). For better understanding of the method and its limitations, we first present a joint spatial-spectral analysis for clustered-dot color halftones and also carry through a 1-D example for which the results are easy to interpret.

3.1 Fourier Analysis of Clustered-Dot Color Halftones

We analyze a general setting where the periodicities of the individual colorant halftones are defined by 2-D lattice tilings of the plane.³⁰ The lattice Λ_i for the i th colorant separation is defined as $\Lambda_i = \{\mathbf{V}_i \mathbf{n} \mid \mathbf{n} \in \mathbb{Z}^2\}$, where \mathbf{V}_i is a 2×2 real-valued matrix, whose columns are the two linearly independent basis vectors that represent the periodicity of the halftone separation, $\mathbf{n} = [n_x \ n_y]^T$, and \mathbb{Z} denotes the set of integers. We first investigated the case where the contone image for the i th colorant, $i \in \{C, M, Y, K\}$, is a constant gray-level image $I_i(x, y) = I_i$, where x and y represent the spatial coordinates along the horizontal and vertical directions, respectively. In this case, the corresponding halftone image corresponds to shifted replicates of a single spot function $s_i(x, y; I_i)$ placed at each point in Λ_i (Refs. 31 to 33). As this halftone is periodic on the lattice, it can be represented in terms of a Fourier series^{31–33} as

$$I_i^h(x, y) = \sum_{n_x=-\infty}^{\infty} \sum_{n_y=-\infty}^{\infty} c_{n_x, n_y}^{I_i} \exp [j2\pi(\mathbf{W}_i \mathbf{n})^T \mathbf{x}], \quad (1)$$

where

$$c_{n_x, n_y}^{I_i} = \frac{1}{|\mathcal{U}_i|} \iint_{\mathcal{U}_i} s_i(x, y; I_i) \exp [-j2\pi(\mathbf{W}_i \mathbf{n})^T \mathbf{x}] dx dy, \quad (2)$$

are the Fourier series coefficients for the halftone spot function $s_i(x, y; I_i)$, the matrix $\mathbf{W}_i = (\mathbf{V}_i^{-1})^T$ includes the two linearly independent fundamental screen frequency vectors

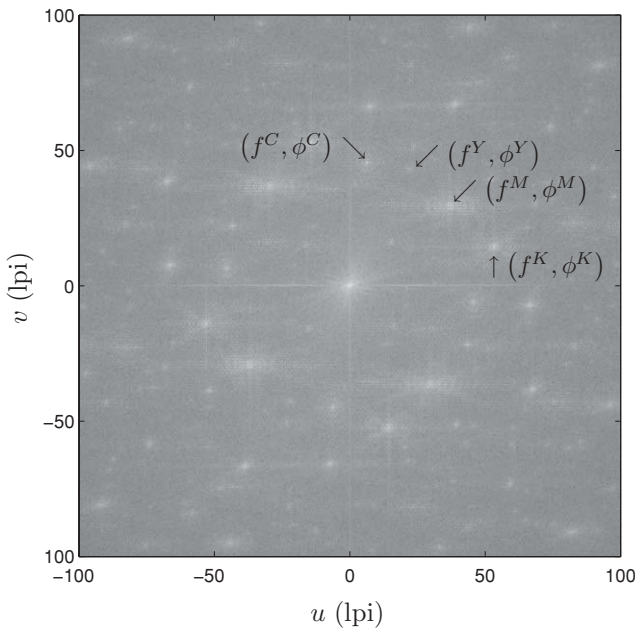


Fig. 5 Enlarged view of the log-magnitude Fourier spectrum of the G channel of the scanned “Hats” halftone print used in our experiments. For illustration purposes, the frequencies of the constituent halftone separations are indicated by arrow and text labels.

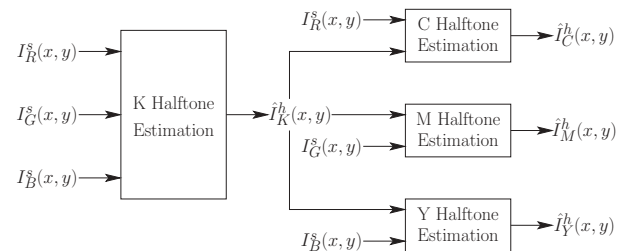


Fig. 6 Overview of $CMYK$ halftone separation estimation using the RGB channels of the scanned image.

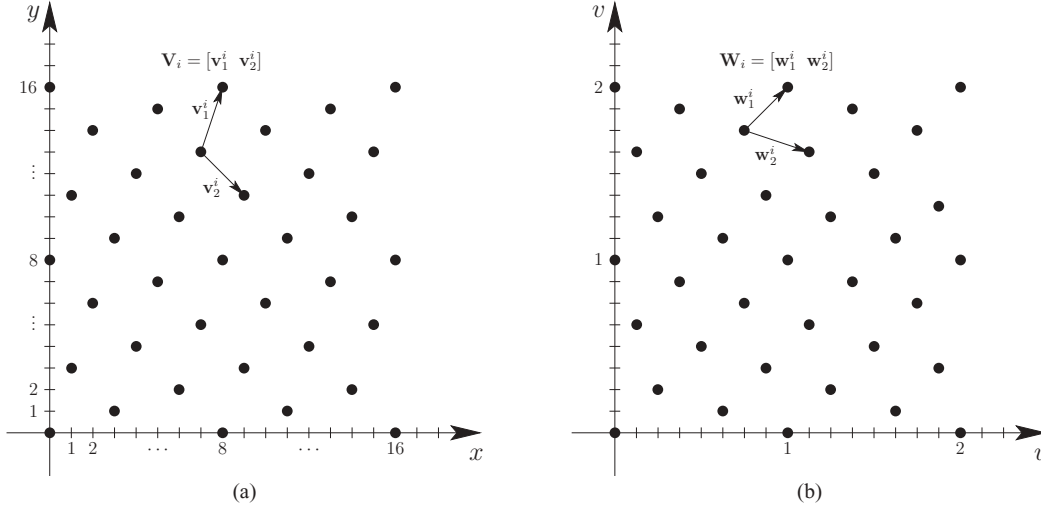


Fig. 7 (a) Example of a halftone periodicity lattice Λ_i and (b) the corresponding reciprocal spatial frequency lattice Λ_i^* .

for the i th halftone separation as its columns, \mathcal{U}_i is the unit cell for the lattice Λ_i and $|\mathcal{U}_i|$ is its area, $\mathbf{n} = [n_x \ n_y]^T$ and $\mathbf{x} = [x \ y]^T$. Recall, that in our notational convention halftone image $I_i^h(x, y)$ values of 1 and 0 correspond, respectively, to regions with and without the i th colorant. The lattice $\Lambda_i^* = \{\mathbf{W}_i \mathbf{n} \mid \mathbf{n} \in \mathbb{Z}^2\}$ constitutes the reciprocal spatial frequency lattice for the lattice Λ_i . The Fourier spectrum of $I_i^h(x, y)$ is comprised of impulses at frequencies $\mathbf{u} \in \Lambda_i^*$, that correspond to the Fourier spectrum of the halftone spot function $s_i(x, y; I_i)$ sampled at $\mathbf{u} = \mathbf{W}_i \mathbf{n}$, where $\mathbf{u} = [u, v]^T$, and u and v represent the frequency coordinates along the horizontal and vertical directions, respectively. To aid understanding, we include in Fig. 7 an illustration of a halftone periodicity lattice Λ_i and its reciprocal spatial frequency lattice Λ_i^* , where the basis vectors corresponding to the columns of \mathbf{V}_i and \mathbf{W}_i are also indicated. Additional illustrations and mathematical details of the representation can be found in Refs. 8, 33, and 34.

A similar representation can be obtained for the halftone image for a contone image with varying image content by decomposing the contone image in the form of a sifting integral and combining it with the Fourier series representation for the halftone for a constant gray level image as^{35,36}

$$I_i^h(x, y) = \sum_{n_x=-\infty}^{\infty} \sum_{n_y=-\infty}^{\infty} c_{n_x, n_y}^{I_i(x, y)} \exp[j2\pi(\mathbf{W}_i \mathbf{n})^T \mathbf{x}], \quad (3)$$

where

$$c_{n_x, n_y}^{I_i(x, y)} = \frac{1}{|\mathcal{U}_i|} \iint_{\mathcal{U}_i} s_i[x, y; I_i(x, y)] \times \exp[-j2\pi(\mathbf{W}_i \mathbf{n})^T \mathbf{x}] dx dy \quad (4)$$

are the Fourier series coefficients for the halftone spot function $s_i[x, y; I_i(x, y)]$ for the image gray-level $I_i(x, y)$. The functions $c_{n_x, n_y}^{I_i(x, y)}$ have spatial frequency bandwidths that are rather small as compared to the frequencies $\mathbf{W}_i \mathbf{n}$, $\mathbf{n} \in \mathbb{Z}^2$. The Fourier spectrum of the halftone image obtained by a Fourier transform of the preceding identity therefore includes the spectrum of the original image (centered at dc) and the spectra of nonlinearly transformed versions $c_{n_x, n_y}^{I_i(x, y)}$ of the original

image generated by the halftoning, each shifted to a corresponding frequency $\mathbf{u} = \mathbf{W}_i \mathbf{n}$, $\mathbf{n} \in \mathbb{Z}^2$ (Refs. 35 and 36).

Having described a model for the individual halftone separations, we now consider an idealized model for the printing and scanning process. For a subtractive color reproduction system³⁷ with transparent (nonscattering) *CMYK* colorants, the reflectance of the *CMYK* halftone overlay can be written as

$$\begin{aligned} r(x, y; \lambda) &= r_W(\lambda) \prod_{i \in \{C, M, Y, K\}} [t_i(x, y; \lambda)]^2 \\ &= r_W(\lambda) \prod_{i \in \{C, M, Y, K\}} [t_i(\lambda)]^2 I_i^h(x, y), \end{aligned} \quad (5)$$

where $t_i(\lambda)$ is the transmittance of the i 'th colorant, and $r_W(\lambda)$ is the reflectance of the paper substrate at wavelength λ . Note that the incoming light is attenuated by traversing each colorant layer twice and also reflected by the paper substrate. The colorant transmittances are further modeled as per the Beer-Bouguer law (Ref. 38, Chap. 7) or the transparent formulation of Kubelka-Munk theory (Ref. 38, Chap. 7) as $[t_i(\lambda)]^2 = 10^{-d_i(\lambda)}$, where $d_i(\lambda)$ is the optical density for the i 'th colorant layer (under to and fro passage). Equation (5) becomes

$$\begin{aligned} r(x, y; \lambda) &= r_W(\lambda) \prod_{i \in \{C, M, Y, K\}} 10^{-d_i(\lambda) I_i^h(x, y)} \\ &= r_W(\lambda) 10^{-\sum_{i \in \{C, M, Y, K\}} d_i(\lambda) I_i^h(x, y)}. \end{aligned} \quad (6)$$

The k 'th color channel of the scanner $I_k^s(x, y)$, $k \in \{R, G, B\}$, measures the fraction of the illuminant light reflected from the print within the transmittance band of the filter k . Using a narrow spectral band assumption for the scanner spectral sensitivities, we approximate the recorded k 'th scanner channel image as

$$I_k^s(x, y) = I_k^s(W) 10^{-\sum_{i \in \{C, M, Y, K\}} d_i(\lambda_k) I_i^h(x, y)}, \quad (7)$$

where the k 'th scanner channel sensitivity is approximated by an impulse (Dirac delta function) at wavelength λ_k , and $I_k^s(W) = r_W(\lambda_k)$ is the scanned image value corresponding

to the paper substrate in the k th color channel. The scanned image values can be converted to density as

$$d(x, y; \lambda_k) = d_k(x, y) = -\log_{10} \left[\frac{I_k^s(x, y)}{I_k^s(W)} \right] \\ = \sum_{i \in \{C, M, Y, K\}} d_k^i I_i^h(x, y), \quad (8)$$

where $d_k^i = d_i(\lambda_k)$ is the optical density of the i 'th colorant layer in the k 'th scanner channel. Note that the density space representation for the scanned images in Eq. (8) avoids interseparation moiré since the colorants combine additively in the density space. On the other hand, moiré would be observed in the reflectance space representation given in Eq. (5) as the colorants combine multiplicatively in the reflectance space. Therefore, interseparation moiré would remain present in typical scanned clustered-dot color halftone images. Even though we recognize that the model is an extremely idealized approximation, use of the model provides an improvement over an alternate *ad hoc* approach as we shall subsequently see.

The constituent contone images $I_i(x, y)$, $i \in \{C, M, Y, K\}$, are band-limited to frequencies significantly smaller than the corresponding fundamental screen frequencies. Hence, most of the energy carried by the individual halftones is concentrated in narrow bands around the corresponding fundamental screen frequencies and lower order harmonics. As the colorants combine additively in the optical density space as per Eq. (8), the intensity of any frequency component in the Fourier spectrum of the overlay can be easily obtained by a weighted linear combination of the corresponding intensities in the Fourier spectra of the constituent halftones, where the weights correspond to the optical densities of the colorants in the scanner channel under consideration. Therefore, the frequency components that carry most of the energy in the individual halftone separations continue to carry (depending on the optical density) a significant portion of the energy in the colorant overlays as well. The interference resulting from the unwanted halftone separations can be eliminated/reduced by removing these frequency components. For this purpose, we utilize narrow-band band-reject filters $H_i(u, v)$ to eliminate the unwanted frequency components of the i 'th separation, where u and v represent the frequency coordinates along the horizontal and vertical directions, respectively. These filters may be efficiently implemented by utilizing the 2-D fast Fourier transform (FFT). Our experimental results indicate that the interference resulting from the unwanted halftone separations is significantly reduced by eliminating the unwanted frequency components in a small circular neighborhood [typically around 3 to 4 lines per inch (lpi) radius] of the corresponding fundamental screen frequencies, their second-order harmonics, and their linear combinations.

Note that in the already described filtering process, we do not want the band-reject filter for the screen frequencies of the i 'th separation to eliminate the frequency components that carry significant portions of energy in the other separations. The band-reject filters described in the preceding paragraph eliminate only the lower order harmonics of the unwanted fundamental screen frequencies. Therefore, unless the frequency components of the desired halftone separation

intersect with the frequencies eliminated by the band-reject filters, these frequencies will be preserved. Note that for 2-D lattices defined in an underlying regular digital grid of pixels, the least common frequency for the separations in consideration is the least common right multiple³⁹ of the basis matrices W_i 's. For rotated halftone orientations, this frequency generally appears at higher order harmonics of the fundamental screen frequencies. Thus, the elimination of lower order harmonics of the halftone corresponding to a colorant does not cause the elimination of any lower order harmonics for the other colorant halftones. Note that this argument and our proposed method are restricted to clustered-dot mutually rotated colorant separations. The argument and the proposed method based on using the differences in spatial periodicities are not applicable, for instance, for dot-on/off-dot orientations.²⁷ For dot-on/off-dot configurations, the halftone separations use the same fundamental screen frequency and spatial filtering to eliminate one colorant halftone will also result in the removal of desired frequency components from other colorant halftones as well.

In the following section, we describe the proposed CMYK halftone separation estimation methodology using the densities of the RGB color channels of the scanned images $d_k(x, y)$, $k \in \{R, G, B\}$. As we proceed, we also provide 1-D illustrative examples that help explain the proposed technique. For a 1-D contone image $I_i(x)$, $i \in \{C, M, Y, K\}$, the halftone spots are rectangular pulses, and for image values normalized between 0 and 1 representing white and black, respectively, the halftone spot for the gray-level $I_i(x)$ is represented as $s_i[x; I_i(x)] = \text{rect}[x/I_i(x)]$. Note that the rectangular spots result from the halftoning process—a conversion from colorant amount to colorant surface coverage in our idealized model. The coefficient in Eq. (4) for this spot function can be computed as $c_n^{I_i(x)} = I_i(x) \text{sinc}[nI_i(x)]$ and Eq. (3) becomes³⁵

$$I_i^h(x) = I_i(x) \left\{ 1 + 2 \sum_{n=1}^{\infty} \text{sinc}[nI_i(x)] \cos[2\pi f_i n x] \right\}, \quad (9)$$

where f_i is the fundamental screen frequency of the i 'th separation. Using this representation, we generate examples of CMYK halftone separations shown in Fig. 8. For our example, we use the frequencies $f_C = 1/3$, $f_M = 1/4$, $f_Y = 1/7$, and $f_K = 1/5$ (in arbitrary units). The estimation process works on the RGB scanner densities shown in Fig. 9, where the optical densities of the CMYK colorants were obtained using the scanned RGB image values of the corresponding colorants measured for the printer used in our experiments. Thus, these do reflect the nonidealities in the printing and scanning process that arise from the colorant interactions and are not simply based on our extremely idealized model of Eq. (8).

3.2 Estimation of K Halftone Separation

All scanner channels are jointly used for the estimation of the K halftone separation as K colorant absorbs nearly uniformly across the three scanner RGB channels and therefore contributes similarly to $d_k(x, y)$, $k \in \{R, G, B\}$. Apart from this use of spectral characteristics, the black (K) halftone separation is estimated by exploiting primarily the spatial characteristics of the halftone separations. The overall estimation process is illustrated in Fig. 10. First, we add the scanner

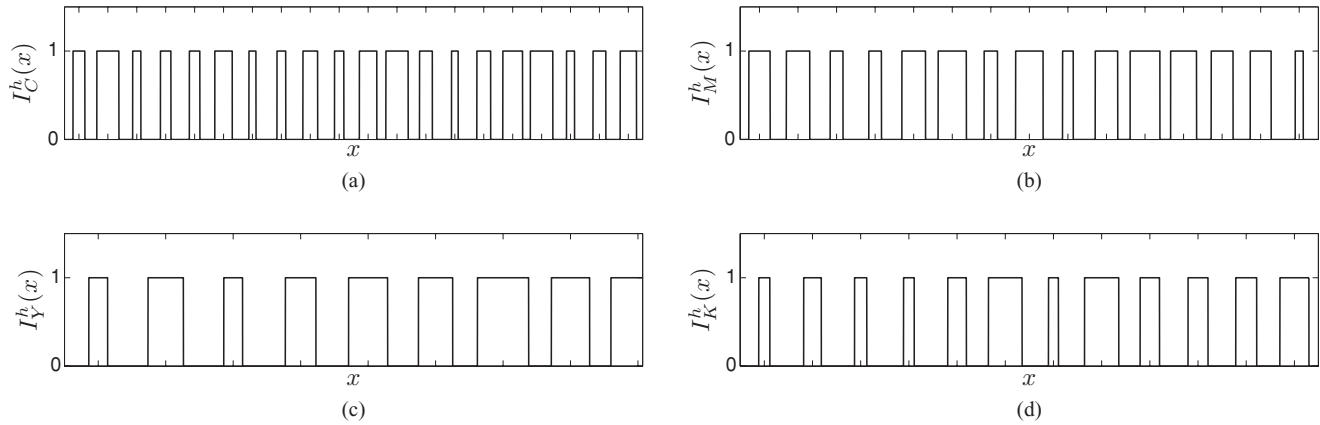


Fig. 8 Sample 1-D halftone patterns for the *CMYK* halftone separations. (a) Cyan; (b) magenta; (c) yellow; and (d) black.

channel densities together in $d_K(x, y) = \sum_{k \in R, G, B} d_k(x, y)$ to obtain a monochrome representation for the scanned image.

There are $2^4 = 16$ possible overlapping combinations of the *CMYK* colorants on the printed paper that are referred to as Neugebauer primaries.³⁷ As the Neugebauer primaries that include the *K* colorant are expected to have larger density than the others, one might consider obtaining the estimate of the *K* halftone from $d_K(x, y)$ by a simple thresholding operation. The accuracy of this approach depends on the optical densities of the individual colorants. Among the eight Neugebauer primaries that include the black (*K*) colorant, the primary with the lowest optical density is the *K* colorant printed alone. Among the remaining eight Neugebauer primaries that do not include the *K* colorant, the overlay of *C*, *M*, and *Y* colorants has the highest optical density. Therefore, to not estimate the overlay of *CMY* colorants as *K* colorant, the constraint

$$\sum_{k \in \{R, G, B\}} d_k^{CMY} < \sum_{k \in \{R, G, B\}} d_k^K \quad (10)$$

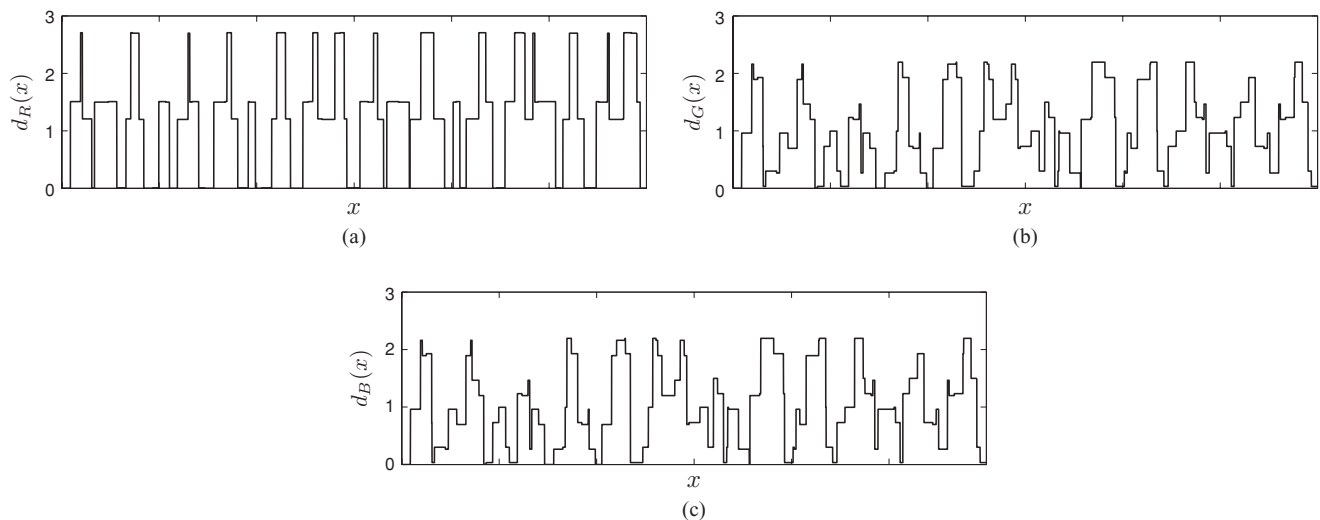


Fig. 9 Predicted *RGB* scanner channel densities for the halftone images shown in Fig. 8. (a) Red; (b) green; and (c) blue.

Scan channel densities

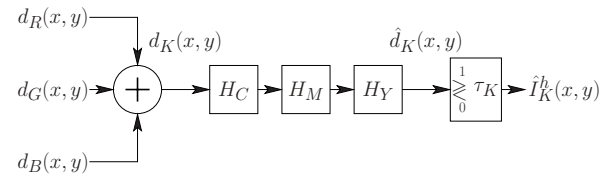


Fig. 10 Detailed overview of *K* halftone separation estimation exploiting the differences in spatial periodicity.

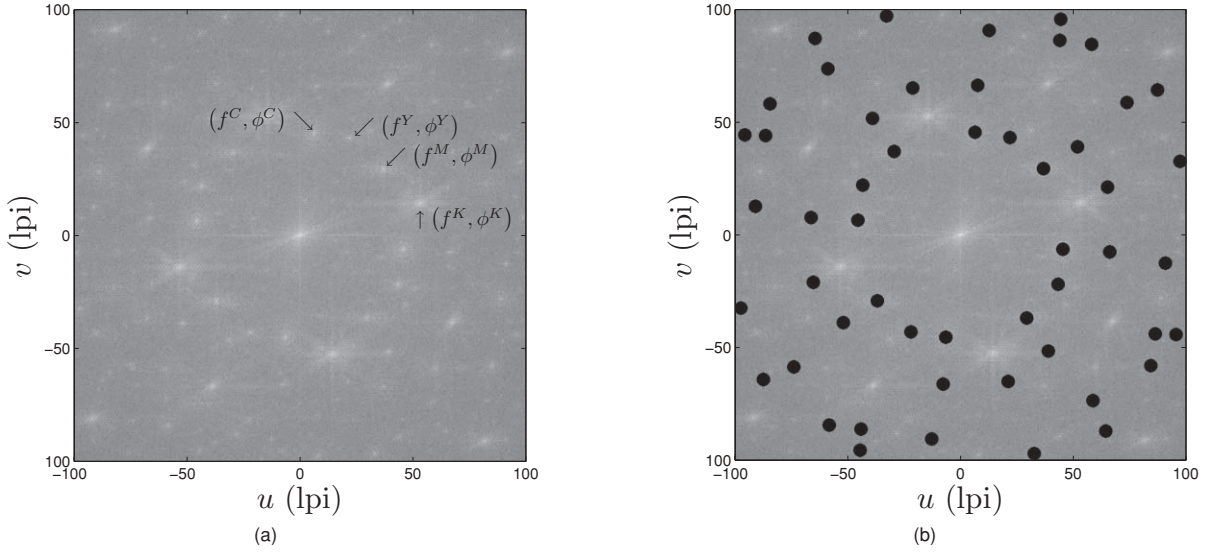


Fig. 11 Spatial filtering for estimation of K halftone $I_K^h(x)$: (a) enlarged view of the log-magnitude Fourier spectrum of $d_K(x, y)$ for the scanned "Hats" print used in our experiments and (b) the elimination of unwanted frequency components of C , M , and Y halftone separations using the narrow-band band-reject filters shown in Figs. 24(a) to 24(c) in Sec. 5, respectively.

must be satisfied, where d_k^{CMY} denotes the density of the overlay of CMY colorants in the k 'th color channel of the scanned image. In most color printing systems, these identities differ by small margins, and estimating the K colorant purely based on spectral differences results in poor performance, as shown in Sec. 3.4, for the printer used in our experiments.

To reduce the interference caused by CMY colorants, we next use the band-reject filters $H_i(u, v)$, $i \in \{C, M, Y\}$, to remove the unwanted frequency components of C , M , and Y halftone separations from $d_K(x, y)$ as

$$\hat{d}_K(x, y) = \mathcal{F}^{-1} \left\{ \mathcal{F}\{d_K(x, y)\} \prod_{i \in \{C, M, Y\}} H_i(u, v) \right\}, \quad (11)$$

where \mathcal{F} denotes the (spatial) Fourier transform operation. Black (K) halftone separation estimate is finally obtained by

$$\hat{I}_K^h(x, y) = \begin{cases} 1 & \text{if } \hat{d}_K(x, y) > \tau_K \\ 0 & \text{otherwise,} \end{cases} \quad (12)$$

where τ_K is a threshold value, which can be taken as the average of the minimum and maximum values in $\hat{d}_K(x, y)$.

Figure 11 illustrates the elimination of the unwanted C , M , and Y halftone structures from the Fourier spectrum of the experimental data using the band-reject filters H_C , H_M , and H_Y shown in Fig. 25 in Sec. 5. The K halftone separation estimate obtained using this method is shown in Fig. 12. Note that the densities $d_K(x, y)$ and $\hat{d}_K(x, y)$ are transformed back to the reflectance space as $I_K^s(x, y)$ and $\hat{I}_K^s(x, y)$ shown in Figs. 12(b) and 12(c), respectively, for a more meaningful representation. In addition, the estimation of K halftone separation using the 1-D densities shown in Fig. 9 is illustrated in Fig. 13. The elimination of the fundamental screen frequencies and the second-order harmonics of the CMY separations is reflected in the

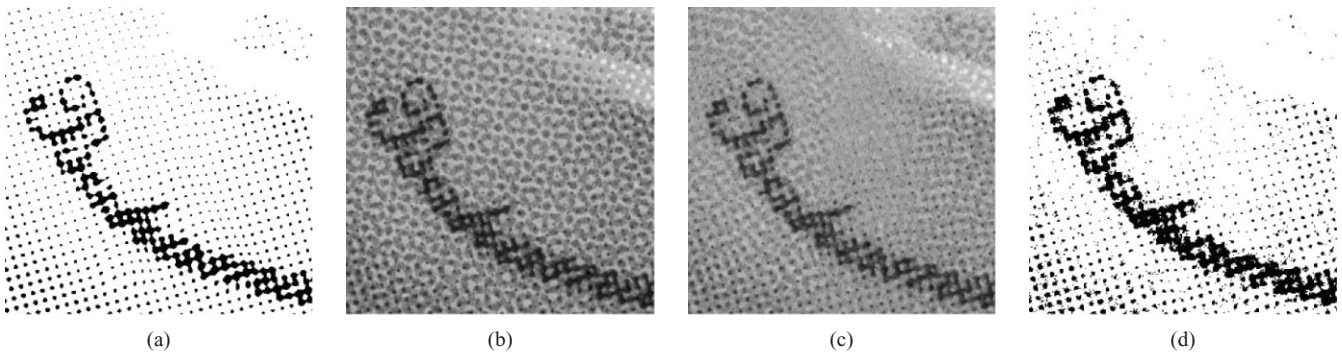


Fig. 12 Sample estimation result for the K halftone separation for the region shown in Fig. 4(c) from the "Hats" halftone image used in our experiments: (a) the digital K halftone separation $I_K^h(x, y)$, (b) the monochrome representation $I_K^s(x, y)$, (c) the filtered image $\hat{I}_K^s(x, y)$, and (d) the K halftone estimate $\hat{I}_K^h(x, y)$.

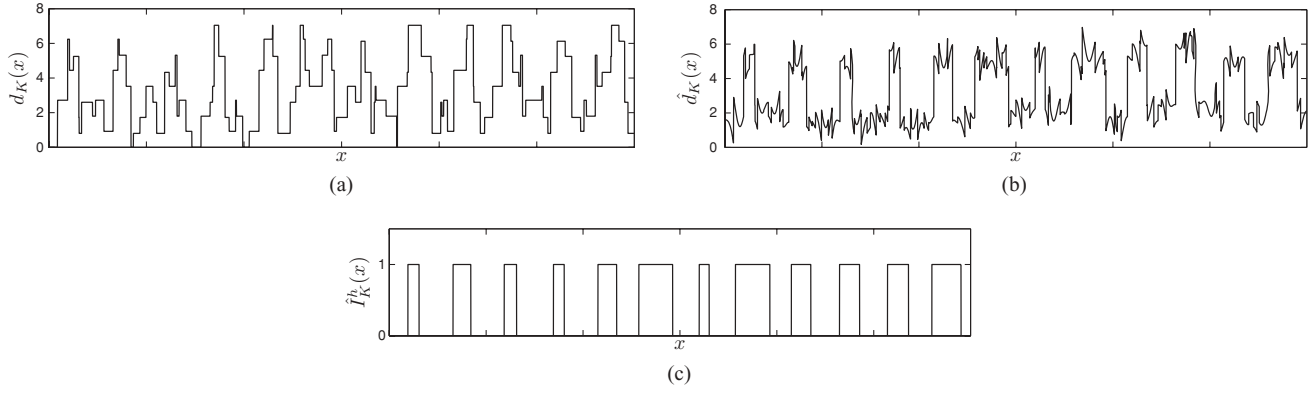


Fig. 13 Illustration of the K halftone separation estimation using the scanner channel densities shown in Fig. 9: (a) the density for the monochrome representation $d_K = \sum_{k \in \{R, G, B\}} d_k$, (b) the filtered density \hat{d}_K , and (c) the K halftone estimate, which matches the original shown in Fig. 8(d).

corresponding representations given in Eq. (9) by changing the lower bound of the summations to $n = 3$.

3.3 Estimation of C , M , and Y Halftone Separations

The efficacy of using the differences in spatial periodicity¹ and colorant spectral differences²⁸ for the estimation of CMY halftone separations from the RGB channels of the scanned images has been shown previously for three-colorant CMY printing. For $CMYK$ printing, however, the black (K) colorant introduces additional challenges so that these methods alone are insufficient to provide accurate estimates.

If the additive in density model of Eq. (8) were exact, the spatial filtering procedure to eliminate undesired halftone separations would provide accurate estimates of the C , M , and Y halftones. However, the actual colorant interactions deviate significantly from the ideal model particularly, at high densities associated with overlaps of the K colorant. As a result, when estimating, for example, the C halftone, removal of the frequency components of the K halftone separation from the RGB scans by spatial filtering also eliminates parts of the C halftone that are overlaid with the K colorant halftone. Thus, spatial filtering alone does not enable recovery of the C , M , and Y halftones. An attempt to separate the halftones based purely on the spectral characteristics (i.e., scanner channel densities) faces similar challenges

because the scanned the image values for the Neugebauer primaries including K differ only by small margins. We, therefore, address this problem by utilizing both techniques jointly, where in addition to the scan RGB channel images, we use the K halftone separation estimate for the estimation of the complementary CMY halftone separations, respectively.

We describe only the estimation of the M halftone separation, with examples illustrating the images obtained during the process. Other halftone separations can be estimated similarly. A detailed overview of the M halftone separation estimation is illustrated in Fig. 14.

The M halftone separation is estimated from its complementary G channel of the scanned image and the K halftone separation estimate obtained previously. First, an estimate of the overlap of M and K halftone separations is obtained by using the G scan channel density $d_G(x, y)$. As the colorants combine additively in the density space, the densities of the Neugebauer primaries that include both M and K colorants is larger than the densities of the constituent colorants. In other words, the overlays that include both M and K colorants will appear darker than the constituent colorants in the G color channel of the scanned image. Using this property, we obtain an estimate of the MK halftone overlap as

$$\hat{I}_{MK}^h(x, y) = \begin{cases} 1 & \text{if } d_G(x, y) > \tau_{MK} \\ 0 & \text{otherwise,} \end{cases} \quad (13)$$

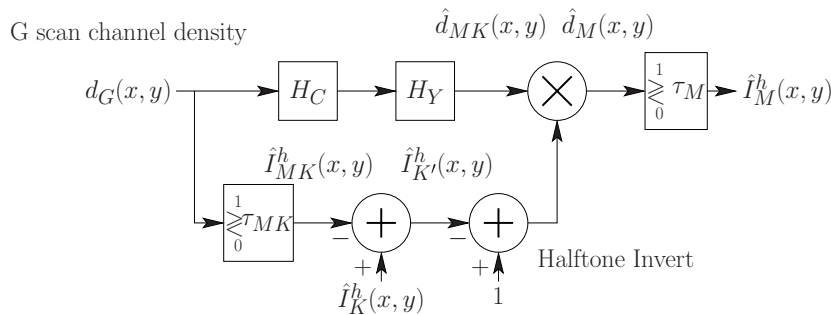


Fig. 14 Detailed overview of M separation estimation using the scanner G channel image and the K separation estimate.

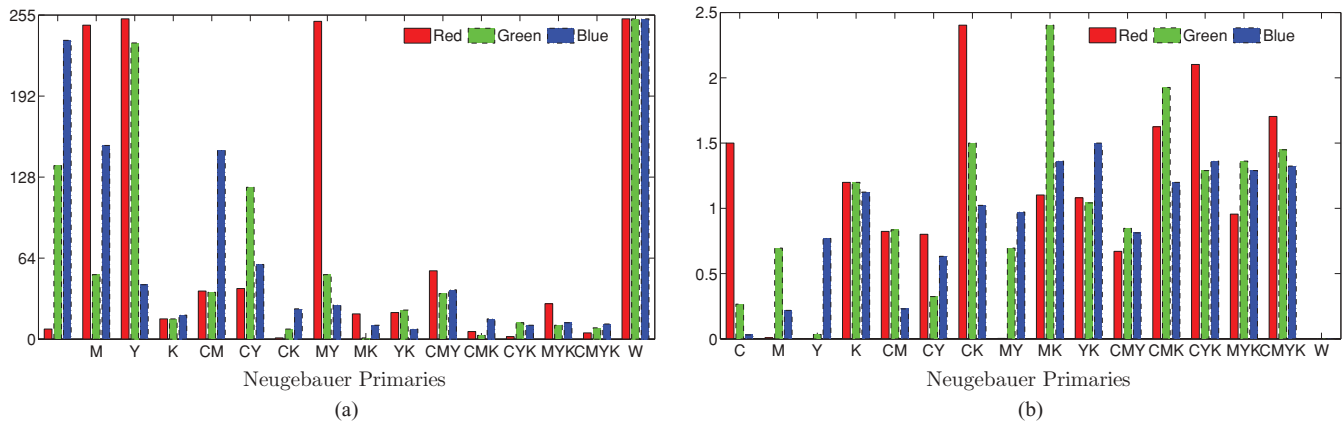


Fig. 15 Scan *RGB* (a) reflectance space and (b) density space values for the 16 Neugebauer primaries for the printer used in our experiments.

where τ_{MK} is a threshold value and, in our convention, the values 1 and 0 correspond, respectively, whether both M and K toners/inks are, or are not, estimated to be deposited at the pixel position (x, y) . The threshold τ_{MK} is chosen midway between the G scanner channel densities for the Neugebauer primaries formed by the MK overlay and that of the M or K (alone) primary, whichever is higher. These densities can be measured from scans by segmenting and averaging interior regions corresponding to the Neugebauer primaries.

The accuracy of this estimation step depends on the optical densities of the individual colorants in the scan G channel. There are four Neugebauer primaries that include both the magenta (M) and black (K) colorants. In this group, the primary with the lowest optical density corresponds

to the overlay of M and K colorants alone. Among the remaining 12 Neugebauer primaries, the overlay of C , M , and Y , and the overlay of C , Y , and K colorants have the highest optical densities. To ensure that these primaries are not incorrectly assigned as the MK Neugebauer primary, the constraints

$$\begin{aligned} d_G^{CMY} &< d_G^{MK} \quad \text{and} \\ d_G^{CYK} &< d_G^{MK} \end{aligned} \quad (14)$$

must be satisfied, where d_G^{CMY} , d_G^{CYK} , and d_G^{MK} are the G channel densities for the Neugebauer primaries corresponding to the overlay of the CMY , CYK , and MK colorants, respectively. In addition, to be able to distinguish the optical density of the overlap of M and K colorants from the optical

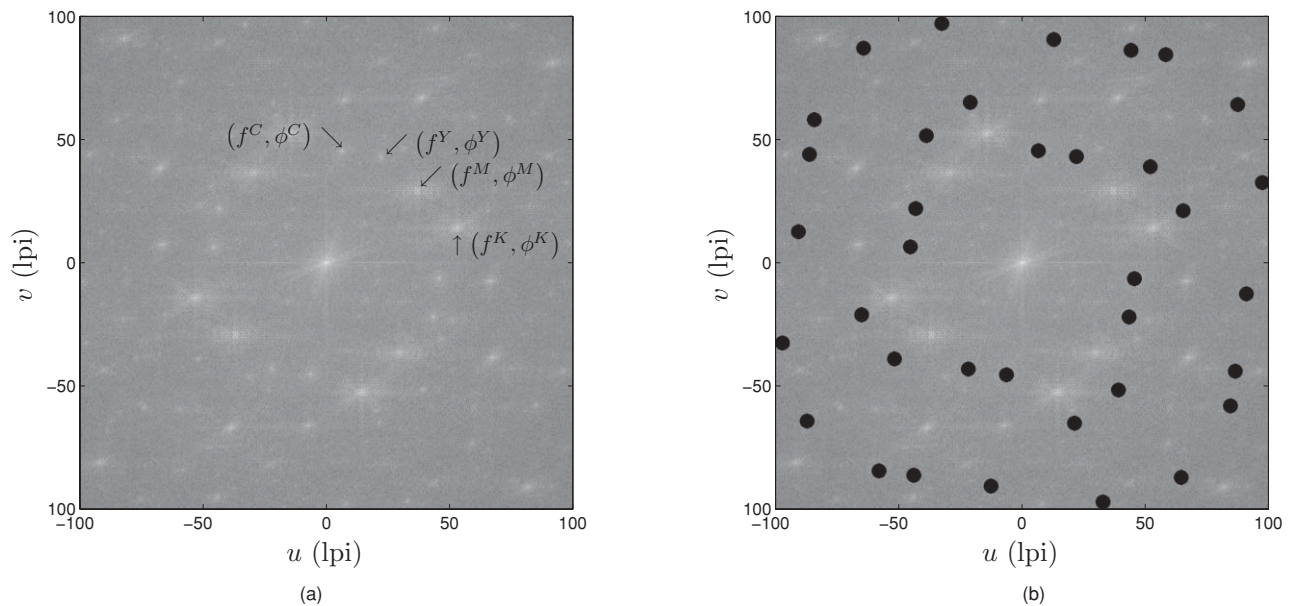


Fig. 16 Spatial filtering for estimation of the density of M and K halftone overlay $\hat{d}_{MK}(x, y)$: (a) enlarged view of the log-magnitude Fourier spectrum of the G scan channel density of the scanned "Hats" halftone print used in our experiments and (b) the elimination of unwanted frequency components of C and Y halftone separations using the band-reject filters shown in Figs. 4(a) and 24(c), respectively.

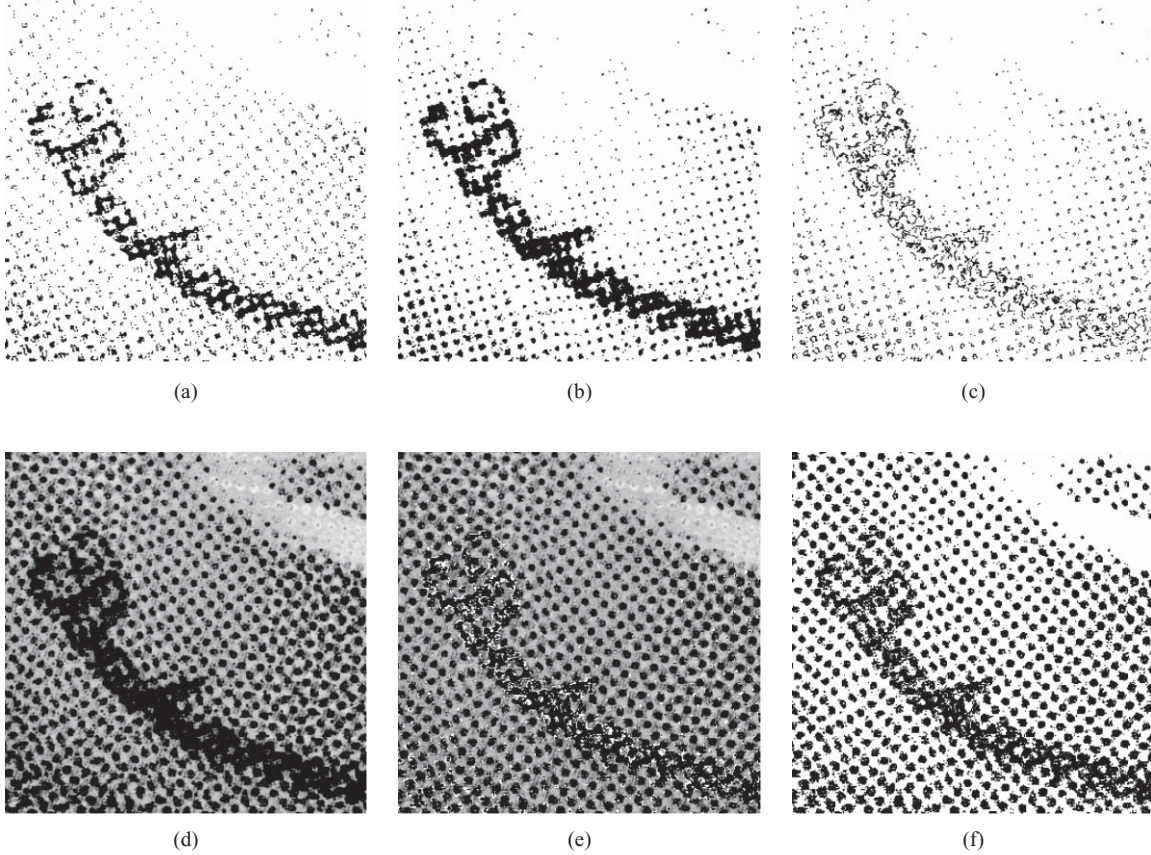


Fig. 17 Images obtained during the estimation of M halftone separation corresponding to the region shown in Fig. 4(d) from the “Hats” halftone image used in our experiments: (a) the estimate of M and K colorant overlap $\hat{I}_{MK}^h(x, y)$, (b) the K halftone estimate obtained previously $\hat{I}_K^h(x, y)$, (c) the estimate of K halftone structures that are not overlapping with M halftone structures $\hat{I}_K^h(x, y)$, (d) the estimate of M and K halftone overlay $\hat{I}_{MK}^s(x, y)$, (e) the image after removing the K only halftone structures by $\hat{I}_K^h(x, y)$ masking $\hat{I}_M^s(x, y)$, and (f) the M halftone estimate $\hat{I}_M^h(x, y)$.

densities of both M and K colorants, neither of the optical densities of the M and K colorants in scan G channel can be ∞ , in other words, neither of the M and K colorants can have perfect absorption, which typically is the case in most color printing systems. This can be observed in the experimental data in Fig. 15(b) that shows the scan RGB values for the 16 Neugebauer primaries for the printer used in our experiments.

Next, the estimate $\hat{I}_{MK}^h(x, y)$ is subtracted from the previously obtained K halftone separation estimate $\hat{I}_K^h(x, y)$ to get an estimate of $\hat{I}_K^h(x, y)$ that represents K halftone structures that are not overlapping with M halftone structures. The unwanted frequency components of C and Y halftone separations are then eliminated from the scan G channel density using the band-reject filters H_C and H_Y , respectively, by

$$\hat{d}_{MK}(x, y) = \mathcal{F}^{-1} \left\{ \mathcal{F}\{d_G(x, y)\} \prod_{i \in \{C, Y\}} H_i(u, v) \right\}. \quad (15)$$

This image approximates the density of the overlay M and K halftone separations in the scanner G channel. Figure 16 illustrates the elimination of the unwanted frequency compo-

nents of C and Y halftone structures in the Fourier spectrum of the density of the G channel of the experimental data using the band-reject filters H_C and H_Y shown in Sec. 5 in Figs. 24(a) and 24(c), respectively.

We then use $\hat{I}_K^h(x, y)$ as a mask to clean out the K halftone structures that do not overlap with M halftone structures from $\hat{d}_{MK}(x, y)$ as $\hat{d}_M(x, y) = \hat{d}_{MK}[1 - \hat{I}_K^h(x, y)]$. The M halftone separation estimate is finally obtained by

$$\hat{I}_M^h(x, y) = \begin{cases} 1 & \text{if } \hat{d}_M(x, y) > \tau_M \\ 0 & \text{otherwise,} \end{cases} \quad (16)$$

where τ_M is a threshold that is set midway between the scanner G channel densities for the M (alone) Neugebauer primary and the CY Neugebauer primary, which has the next higher density.

We previously showed in Fig. 4(e) a sample estimate for the M halftone separation using the G color channel of the scanned image shown in Fig. 4(d) and the K halftone estimate shown in Fig. 12(d). To illustrate the method, the images obtained in intermediate stages of the proposed estimation process are shown in Fig. 17. Note that the densities $\hat{d}_{MK}(x, y)$ and $\hat{d}_M(x, y)$ are transformed back to the reflectance space as $\hat{I}_{MK}^s(x, y)$ and $\hat{I}_M^s(x, y)$ shown in Figs. 17(d) and (e),

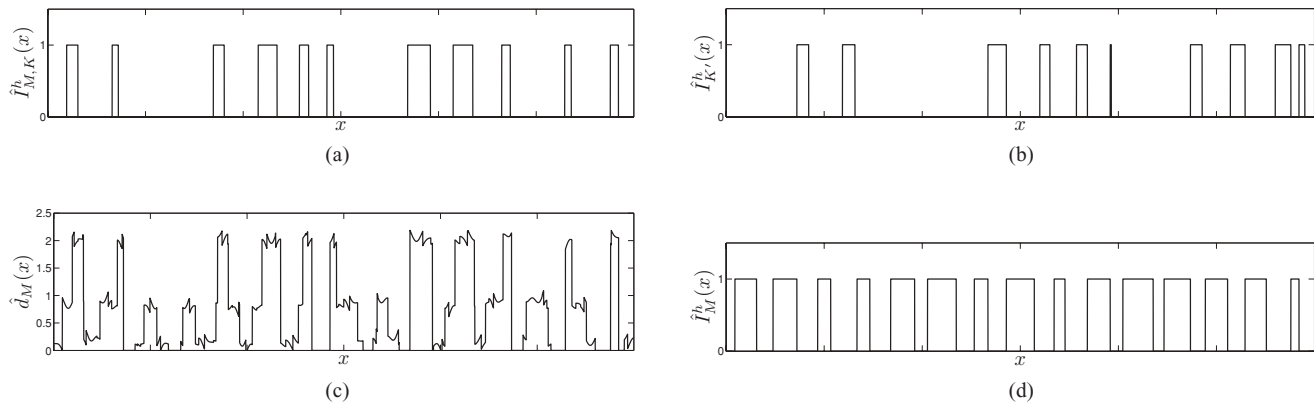


Fig. 18 Illustration of the M halftone separation estimation using the density shown for the G scan channel in Fig. 9(b) and the K halftone estimate shown in Fig. 13(c): (a) the estimate of MK halftone overlap, (b) the estimate of K halftone separation not overlapping with M halftone, (c) the filtered density \hat{d}_{MK} multiplied by $[1 - \hat{I}_K^h(x)]$, and (d) the M halftone estimate, which matches the original shown in Fig. 8(b).

respectively, for a more meaningful representation. In addition, the estimation of M halftone separation using the 1-D scan G channel density shown in Fig. 9(b) and the previously obtained K halftone estimate shown in Fig. 13(c) is illustrated in Fig. 18. The elimination of the fundamental screen frequencies and the second-order harmonics of the C and Y separations is reflected in the corresponding representations given in Eq. (9) by changing the lower bound of the summations to $n = 3$.

3.4 Performance Analysis: Accuracy of the Estimated Halftones

Given the dot gain and the geometric distortion in the printing and other nonidealities in the print-scan process, it is difficult to experimentally evaluate the performance of the estimation process quantitatively. Therefore, we utilize a simulation framework, where the effect of print-scan is simulated by the Neugebauer model³⁷ and spatial blur. The overview of the simulation is shown in Fig. 19. First, the individual colorant separations of the contone image $I_{C,M,Y,K}(x, y)$ are halftoned. Next, the effect of the print-scan is simulated on the digital halftone $I_{C,M,Y,K}^h(x, y)$. Estimates of the halftone separations $\hat{I}_{C,M,Y,K}^h(x, y)$ are then obtained from $I_{R,G,B}^s(x, y)$ using our methodology, and finally, the performance metrics for the estimates of each separation are calculated.

Twenty-four images from the Kodak PhotoCD image set, as shown in Fig. 20, were used in our simulations. The $CMYK$ versions of these images were obtained using Adobe® Photoshop® CS4 with default $CMYK$ settings. We then generated clustered-dot halftones for these images in 3.84×2.56 -in. format for a 600 dots per inch (dpi) $CMYK$ color printer. Digital rotated clustered-dot $CMYK$ halftone screens with angular orientations close to the conventional singular moiré-free 15-, 75-, and 45-deg rotated clustered-dot halftones were utilized for our simulations.⁴⁰ The fundamental frequency vectors for these screens are shown in Fig. 21. Since the objective was to evaluate the accuracy of the estimated halftones, no watermarks were utilized in these simulations.

The effect of print-scan is simulated for a 600 dpi $CMYK$ color printer and RGB color scanner combination. For this purpose, we utilize a Neugebauer model³⁷ in scanner RGB space. Binary $CMYK$ printer values are mapped to contone RGB scanner values through a look-up table (LUT) transformation. For this purpose, the average RGB values of 16 Neugebauer primaries for the printer used in our experiments were measured from 0.5×0.5 -in.² printed patches and stored in the LUT. Figure 15(a) shows the measured scan RGB values for the 16 Neugebauer primaries. The $CMYK$ values of each pixel in the color halftone are mapped to the RGB scanner values using the LUT. Note that since we use actual measured values, spectral nonidealities in the colorant

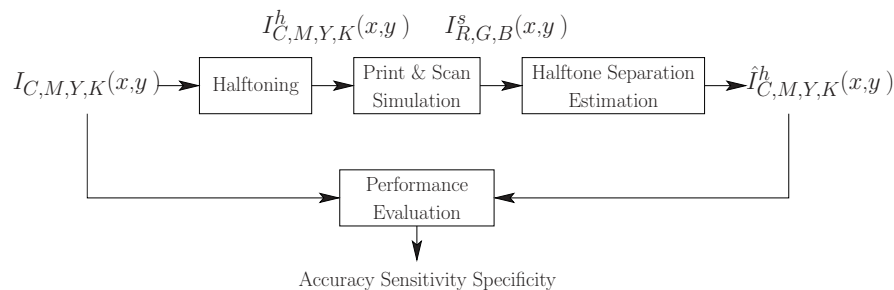


Fig. 19 Simulation model for evaluating the performance of the estimation process.

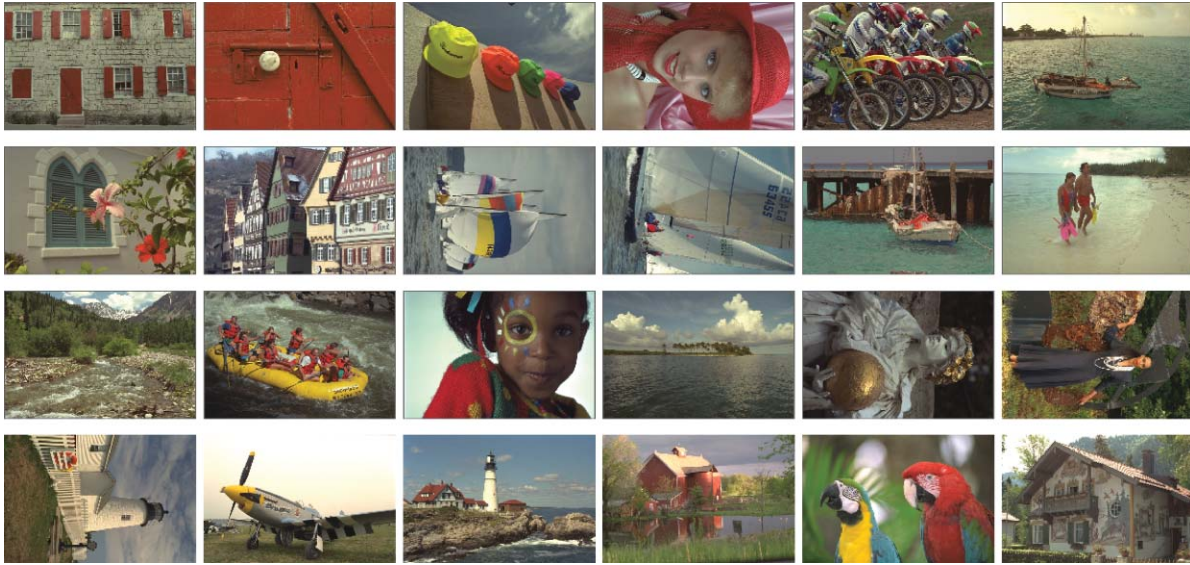


Fig. 20 Kodak PhotoCD image set used in the simulations. These images are referred to as Image 1 to Image 24, enumerated from left-to-right and top-to-bottom, respectively.

interactions and in the scanner response are automatically incorporated in the modeling process. To also model spatial nonidealities, we performed a spatial blur on the individual *RGB* channels of the resulting image, analogous to the methodology of Ref. 41. For this purpose, a 7×7 Gaussian low-pass filter (DC response normalized to 1) with standard deviation approximately equal to 0.96 pixels was employed. For the 600-dpi printer resolution we assumed, this corresponds to a standard deviation of $40 \mu\text{m}$, and the blur causes spreading in an approximately $120 \mu\text{m}$ radius. Note that a more severe blur increases the impact of the spatial interactions, and consequently, the accuracy of the estimates would decrease. Similarly, a milder blur brings the simulation closer to a spatially ideal hard-dot setting,^{42,43} and thus, the accuracy of the estimates would be higher.

Using the described methodology, we obtained estimates of the individual halftone separations. The band-reject filters designed for these frequency vectors are shown in Fig. 22. For purpose of visual comparison, enlarged views of the original *CMYK* halftone separations and their estimates from a region in Image 3 in Fig. 20 (also referred to as the “Hats” image in the remaining parts of this paper) are shown in Fig. 23.

The performance of the described halftone separation estimation methodology is evaluated by the accuracy, sensitivity, and specificity, which are common performance measures for binary data classification techniques.⁴⁴ In our context, they represent the percentage of overall, majority, and minority pixels that are correctly classified, respectively, and are computed for each colorant as

$$\begin{aligned} \text{accuracy} &= \frac{N_{tp} + N_{tn}}{N_{tp} + N_{tn} + N_{fp} + N_{fn}} \times 100, \\ \text{sensitivity} &= \frac{N_{tp}}{N_{tp} + N_{fn}} \times 100, \\ \text{specificity} &= \frac{N_{tn}}{N_{tn} + N_{fp}} \times 100, \end{aligned} \quad (17)$$

where N_{tp} is the number of true positive predictions corresponding to number of majority pixels that are predicted correctly, N_{tn} is the number of true negative predictions corresponding to number of minority pixels that are predicted correctly, N_{fp} is the number of false positive predictions corresponding to the number of minority pixels that are predicted as majority, and N_{fn} is the number of false negative predictions corresponding to the number of majority pixels that are predicted as minority. The estimation performance for each colorant is listed in Table 1. Around 95% accuracy is achieved for *C*, around 98% accuracy is achieved for *K* halftone separations, and relatively lower accuracies are achieved for the *M* and *Y* halftone separations. This difference is caused by the varying levels of spectral interference observed in the scanner *RGB* channels. As we can see in Fig. 2, relatively less interference is observed in the scanner *R* channel compared to the *G* and *B* channels. Therefore, the *C* and *K* halftone separations can be estimated better than the *M* and *Y* halftone separations. Nevertheless, as we demonstrate later in Sec. 5, these estimates enable successful detection of the embedded watermark patterns.

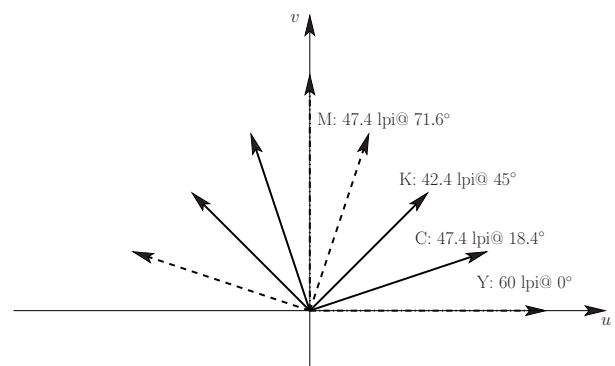


Fig. 21 Frequency vectors for singular moiré-free *C*, *M*, *Y*, and *K* halftone screens.

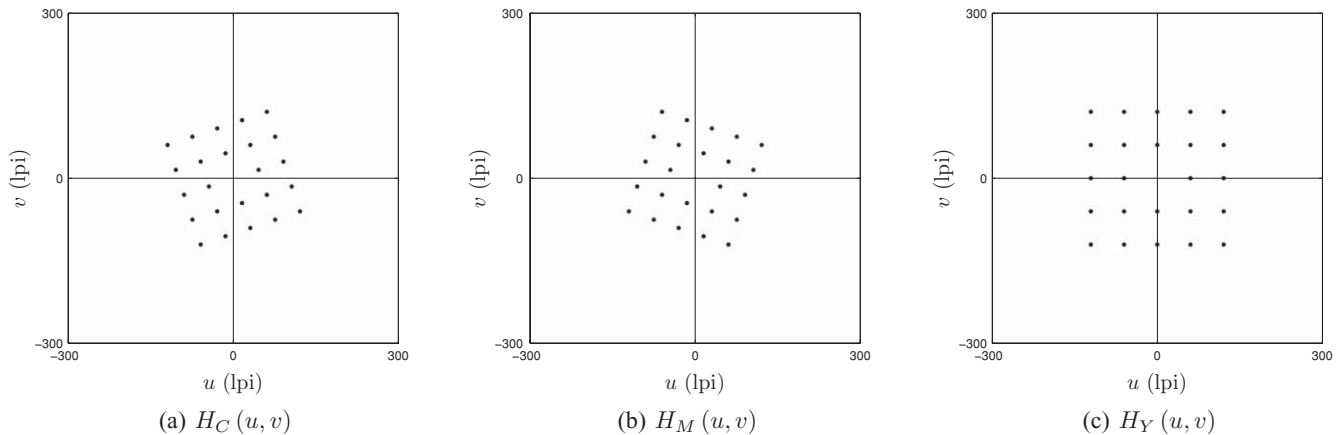


Fig. 22 Narrow-band band-reject filters for eliminating the frequency components of the *CMY* halftone separations from the densities of the *RGB* color channels of the scanned images for the frequency vector configuration shown in Fig. 21. (a) cyan, (b) magenta, and (c) yellow.

We compared our methodology against three other estimation methods. The first estimation method is based purely on colorant spectral differences. All scanner channels are jointly used for the estimation of *CMYK* halftone separations. For a *CMYK* printed and *RGB* scanned image, the histogram in the 3-D *RGB* space is expected to have 16 distinct points corresponding to the 16 Neugebauer primaries. Due to the print-scan nonidealities, however, the histogram typically exhibits scattered points that form clusters around each of the Neugebauer primaries. With this motivation, we employed a vector-quantization-based estimation technique^{45,46} to obtain the constituent halftone separations. For each pixel in the print-scan simulated halftone image, the pixel is classified to the Neugebauer primary to which the pixel values are closest in terms of Euclidean distance in *RGB* coordinates. Individual halftone separation estimates were obtained by transforming the Neugebauer primary indices to corre-

sponding binary halftone separations. The *RGB* values of the Neugebauer primaries for the printer used in our experiments were previously shown in Fig. 15(a). The performance of this methodology for the image set in Fig. 20 is listed in Table 2. It is readily seen that the performance of our proposed methodology is better than the VQ-based estimation technique. Specifically, for the *C* colorant, our method provides significantly better estimates. For this colorant we see that the VQ algorithm misclassifies some of the pixels that include the *C* colorant as *K* and the ones that include the *Y* colorant as the *CMY* overlay for the data from the printer used in our experiments.

The second method is based purely on spatial filtering. The estimation process of the *K* halftone separation is the same as our method. For the estimation of the *C*, *M*, and *Y* halftone separations, the unwanted frequency components of *K* halftone separation are also eliminated by a corresponding

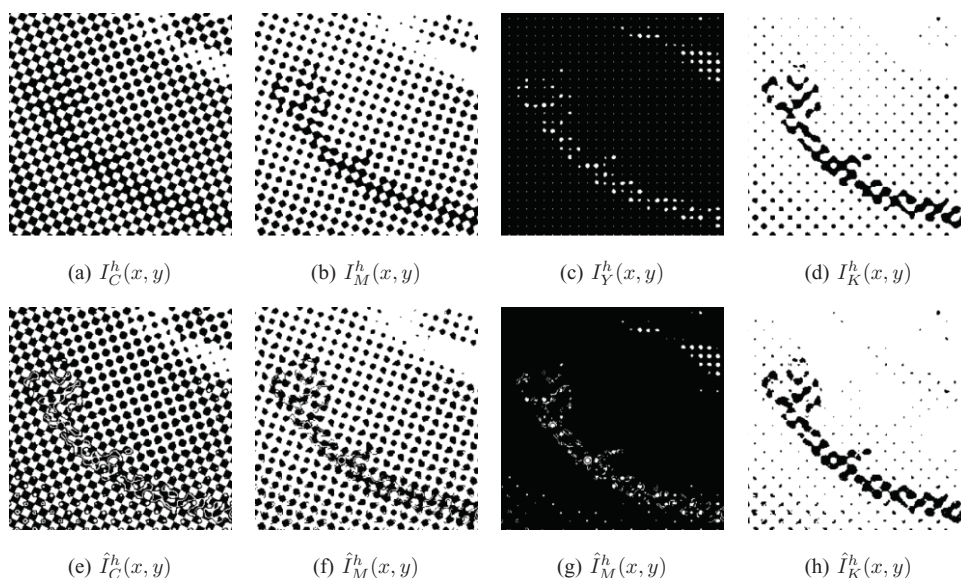


Fig. 23 Enlarged view of the digital halftone separations: (a) to (d) from a region in the “Hats” image and (e) to (h) the corresponding estimates obtained using the differences in spatial periodicity and colorant spectra. (a) and (e), cyan; (b) and (f), magenta; (c) and (g), yellow; (d) and (h), black.

Table 1 Performance of the proposed halftone separation estimation methodology for the image set shown in Fig. 20.

Image No.	Accuracy (%)				Sensitivity (%)				Specificity (%)			
	<i>C</i>	<i>M</i>	<i>Y</i>	<i>K</i>	<i>C</i>	<i>M</i>	<i>Y</i>	<i>K</i>	<i>C</i>	<i>M</i>	<i>Y</i>	<i>K</i>
1	95.5	89.6	90.4	97.8	97.4	87.8	97.0	99.4	93.3	91.6	78.1	97.8
2	95.6	94.1	96.5	99.1	99.3	96.4	99.2	99.5	86.6	83.0	54.8	99.1
3	95.4	88.8	90.6	97.5	93.3	92.4	97.4	99.1	97.5	85.2	78.0	97.5
4	95.7	91.4	89.7	98.1	98.1	95.8	97.8	99.6	91.8	82.9	74.8	98.1
5	93.2	85.6	86.1	98.1	89.3	91.4	94.7	98.9	97.8	78.1	70.6	98.1
6	96.4	90.1	91.4	98.1	98.2	90.8	96.5	99.5	94.3	88.8	84.1	98.1
7	95.2	88.4	90.4	97.0	93.8	86.2	97.3	99.2	96.5	91.0	75.8	97.0
8	95.3	90.0	88.3	97.9	97.9	88.7	82.9	99.3	92.3	91.5	94.6	97.9
9	97.0	92.9	91.5	96.8	96.9	93.7	88.8	99.4	97.1	91.5	94.8	96.8
10	96.6	91.4	89.5	97.1	96.1	90.9	84.9	99.2	97.2	92.2	94.5	97.1
11	94.7	87.6	87.9	96.9	93.2	83.7	95.7	99.0	96.6	91.6	75.5	96.9
12	98.5	94.9	96.5	99.3	99.2	97.2	95.3	99.9	97.3	88.1	97.6	99.3
13	94.6	86.4	90.8	98.1	91.4	85.1	96.6	99.2	97.7	88.0	78.1	98.1
14	94.4	86.6	88.4	98.1	91.4	92.0	96.1	99.3	97.6	80.9	71.7	98.1
15	94.7	89.7	88.5	98.5	98.6	85.1	94.6	99.3	89.3	94.3	81.1	98.5
16	94.9	87.3	88.1	97.3	93.4	83.7	95.3	99.1	96.9	91.6	78.7	97.3
17	93.5	84.5	85.0	97.8	91.2	93.4	93.9	99.2	96.7	73.8	71.7	97.8
18	92.4	82.6	87.7	98.0	88.5	91.5	96.5	98.7	97.7	71.0	62.0	98.0
19	95.7	88.8	91.3	97.3	97.5	87.6	96.1	99.2	93.8	90.4	84.8	97.3
20	96.9	92.1	93.9	99.1	99.3	92.9	93.4	99.7	89.9	89.8	94.9	99.1
21	96.4	90.9	91.7	97.8	95.1	90.0	87.9	99.5	97.9	91.9	95.6	97.8
22	95.9	88.6	91.3	98.3	98.0	86.9	96.8	99.5	93.6	90.7	80.9	98.3
23	96.0	89.2	91.8	98.1	98.3	87.2	97.1	99.4	93.4	91.4	78.3	98.1
24	94.7	87.2	87.9	98.1	92.0	83.8	96.0	99.4	97.4	91.3	76.6	98.1

band-reject filter $H_K(u, v)$ from the complementary R , G , and B scanner channels. The performance of this methodology for the image set in Fig. 20 is listed in Table 3. The estimates for the C , M , and Y colorants are generally less accurate than the ones obtained using the proposed joint approach. This is due to the nonidealities observed in practice, as described in Sec. 3.3.

The last method was used in our preliminary work on this problem.² It simply uses the methods described in Secs. 3.2 and 3.3 with the distinction that the images are processed in the reflectance space instead of the density space processing suggested by our model. The accuracy for the reflectance-space-based estimation method and the improvement with the density space processing is listed in Table 4. We can see that processing the images in the optical density space

generally provides better estimates. Specifically, the accuracy for the K halftone estimates is significantly higher with the processing in density. The estimates for the M and Y halftones show smaller improvements, whereas those for the C halftones show no major improvement.

4 Color Halftone Watermarking using CPM

Having described the overall framework in a general setting, we next demonstrate a specific and concrete instantiation based on CPM for monochrome watermark embedding.²¹ In this specific instantiation, the watermarks w_i can be thought of as visual patterns represented as low-bandwidth (in comparison with the halftone frequency) images. Large-font text

Table 2 Performance of the vector-quantization (VQ)-based halftone separation estimation method for the image set shown in Fig. 20.

Image No.	Accuracy (%)				Sensitivity (%)				Specificity (%)			
	<i>C</i>	<i>M</i>	<i>Y</i>	<i>K</i>	<i>C</i>	<i>M</i>	<i>Y</i>	<i>K</i>	<i>C</i>	<i>M</i>	<i>Y</i>	<i>K</i>
1	83.9	87.2	86.7	90.2	80.3	84.3	96.6	98.9	87.9	90.4	68.4	58.2
2	81.6	90.9	95.4	87.4	82.5	97.5	98.5	99.1	79.2	57.9	46.8	54.3
3	83.3	85.6	85.6	90.7	87.2	89.5	94.7	98.8	79.2	81.7	68.8	64.8
4	83.3	89.3	87.2	89.6	82.1	95.7	95.8	98.9	85.3	76.7	71.4	59.4
5	77.7	83.4	84.1	89.5	80.7	87.9	89.6	99.0	74.0	77.7	74.2	73.9
6	86.3	89.3	89.2	93.5	86.1	90.4	95.5	98.3	86.4	86.9	80.2	64.5
7	84.6	87.0	85.6	91.3	87.8	86.5	96.3	98.6	81.4	87.6	63.1	61.6
8	85.3	86.6	86.4	92.1	84.8	85.3	83.5	97.9	86.0	88.1	89.7	64.9
9	91.4	88.5	89.6	94.9	93.9	88.5	87.5	98.2	88.7	88.4	92.1	51.1
10	88.5	86.9	87.1	93.3	92.5	86.5	81.6	99.1	83.4	87.4	93.1	55.5
11	81.5	84.8	82.9	90.4	86.9	82.0	92.2	99.2	74.1	87.7	67.9	69.0
12	94.3	93.8	92.7	97.3	95.2	95.3	90.4	99.3	92.7	89.4	95.0	62.5
13	80.7	85.9	87.4	90.1	83.2	84.7	94.3	98.5	78.1	87.5	72.2	66.2
14	81.0	85.2	85.7	90.9	82.9	88.1	92.4	98.9	79.0	82.2	71.4	72.7
15	82.5	88.1	87.2	92.2	84.8	86.5	87.5	99.2	79.4	89.7	86.7	78.1
16	82.3	84.5	85.3	91.4	86.6	82.4	91.8	99.3	76.7	86.8	76.8	67.7
17	79.1	82.0	82.3	90.7	82.4	85.6	85.9	99.1	74.6	77.5	76.7	78.6
18	74.0	82.0	84.0	89.2	77.0	86.7	89.2	98.7	69.9	75.9	68.7	77.3
19	85.1	85.7	86.5	91.3	81.8	82.8	92.9	98.7	88.5	89.3	77.8	60.2
20	89.6	92.2	91.8	95.4	92.8	94.0	93.8	99.0	79.9	86.3	88.3	74.3
21	87.1	87.5	89.8	93.6	91.0	85.9	88.6	98.6	82.5	89.5	90.9	65.1
22	84.1	87.7	89.0	91.6	81.5	85.1	94.9	97.9	86.8	90.8	77.9	62.8
23	84.0	89.0	90.5	92.2	82.6	86.3	95.4	98.2	85.5	92.0	77.9	66.0
24	81.5	85.7	86.5	90.7	84.3	83.4	93.1	98.7	78.6	88.4	77.2	66.9

rendered as a bilevel image is one example of such visual patterns that we utilize for our illustration.

Continuous phase-modulated halftoning²¹ alters the halftone phase through a modulation of the phase of an underlying analytic halftone threshold function. For watermarking applications, this method is similar to other phase-shift-based clustered-dot halftone watermarking methods^{12,15,17} but has the advantage that the watermark pattern may be decided on dynamically just prior to halftoning, as opposed to the alternative embedding strategies where the pattern must be incorporated in the design of the halftone thresholds, which are therefore static. For completeness, we briefly summarize the embedding process here in our specific context of color halftoning. The halftone for the i 'th separation, $I_i^h(x, y)$ is

assumed to be obtained by comparing the contone image values $I_i(x, y)$ against a periodic halftone threshold function $T_i(x, y)$ as

$$I_i^h(x, y) = \begin{cases} 1 & \text{if } I_i(x, y) < T_i(x, y) \\ 0 & \text{otherwise.} \end{cases} \quad (18)$$

To describe our watermark embedding technique, we use a modified version of the analytic description proposed by Pellar and Green⁴⁷ and Pellar.⁴⁸ We assume that the fundamental screen frequency for the i 'th halftone separation, $i \in \{C, M, Y, K\}$, is f_i lpi that is oriented along the angle ϕ_i . This description assumes orthogonal halftones, where

Table 3 Performance of the spatial-filtering-based halftone separation estimation method for the image set shown in Fig. 20.

Image No.	Accuracy (%)				Sensitivity (%)				Specificity (%)			
	<i>C</i>	<i>M</i>	<i>Y</i>	<i>K</i>	<i>C</i>	<i>M</i>	<i>Y</i>	<i>K</i>	<i>C</i>	<i>M</i>	<i>Y</i>	<i>K</i>
1	87.7	86.7	87.6	97.8	87.6	82.7	97.8	99.4	87.8	91.0	68.8	92.3
2	80.5	92.5	96.7	99.1	93.2	98.4	99.8	99.5	49.3	63.4	49.1	97.9
3	84.6	81.5	85.0	97.5	94.3	90.4	96.2	99.1	74.3	72.4	64.2	93.0
4	80.7	86.0	87.4	98.1	75.2	93.5	98.0	99.5	89.7	71.5	68.0	93.9
5	81.3	80.4	84.9	98.0	96.0	94.6	98.2	98.8	63.7	62.4	61.1	96.8
6	89.8	82.9	88.7	98.1	85.2	81.3	98.4	99.5	95.0	86.0	74.8	91.6
7	86.7	83.2	86.7	97.0	93.8	76.9	98.0	99.2	79.5	90.8	62.9	89.4
8	88.8	85.9	84.8	97.9	82.5	80.0	75.0	99.3	96.1	93.2	96.1	93.1
9	92.3	89.8	87.1	96.8	96.3	88.0	80.6	99.5	88.1	92.5	95.1	73.6
10	90.4	84.9	83.1	97.1	94.3	82.8	73.2	99.2	85.7	88.0	93.9	85.2
11	84.4	81.3	82.5	96.9	94.8	73.0	94.5	98.9	70.3	89.7	63.3	92.3
12	93.7	94.9	94.8	99.3	92.0	94.3	92.6	99.9	96.7	96.6	97.0	91.5
13	84.5	80.4	90.2	98.0	94.4	72.4	99.1	99.2	74.6	91.2	71.0	95.2
14	83.6	81.0	86.6	98.0	95.5	93.7	98.3	99.2	71.2	67.8	61.5	95.6
15	83.0	86.1	87.6	98.5	73.6	76.4	98.0	99.3	95.9	95.9	75.1	97.1
16	86.2	80.1	83.0	97.3	94.9	73.2	93.6	99.1	75.0	88.2	69.2	92.1
17	81.0	78.2	83.0	97.7	95.7	93.9	96.8	99.1	61.0	59.1	62.3	95.9
18	79.5	75.4	88.0	97.9	96.0	94.5	99.5	98.7	57.3	50.8	54.3	97.1
19	86.7	82.8	85.4	97.3	79.0	76.0	92.2	99.2	94.8	91.1	76.4	90.4
20	91.3	88.9	93.9	99.1	90.2	88.4	91.0	99.7	94.6	90.5	98.7	96.4
21	89.1	87.8	90.1	97.8	96.2	83.3	82.4	99.5	80.6	93.7	98.1	90.4
22	85.2	80.7	90.5	98.3	77.9	74.4	98.6	99.5	93.3	88.2	75.4	94.1
23	86.2	81.9	91.4	98.1	78.8	75.4	99.0	99.5	94.4	89.1	72.1	93.6
24	84.6	79.7	85.3	98.0	93.7	72.3	97.6	99.3	75.3	88.5	68.3	94.7

the matrix of frequency vectors for each halftone separation is composed of two orthogonal vectors of equal length. Note that more general descriptions are also possible.³³ Then, assuming input continuous tone image values that are normalized to range between -1 and 1 , the corresponding threshold function for the i 'th separation is

$$T_i(x, y) = \cos\left(2\pi \frac{f_i}{\sqrt{2}}x'\right) \cos\left(2\pi \frac{f_i}{\sqrt{2}}y'\right), \quad (19)$$

where

$$\begin{bmatrix} x' \\ y' \end{bmatrix} = \begin{bmatrix} \cos(\phi_i - \frac{\pi}{4}) & -\sin(\phi_i - \frac{\pi}{4}) \\ \sin(\phi_i - \frac{\pi}{4}) & \cos(\phi_i - \frac{\pi}{4}) \end{bmatrix} \begin{bmatrix} x \\ y \end{bmatrix}. \quad (20)$$

A watermark pattern is embedded in the halftone by modulating the phase of one of the cosine function arguments by incorporating a spatially varying phase function $\Psi_i(x, y)$, which enables phase variations along the corresponding halftone orientation. The modified version of the halftone threshold function is given by

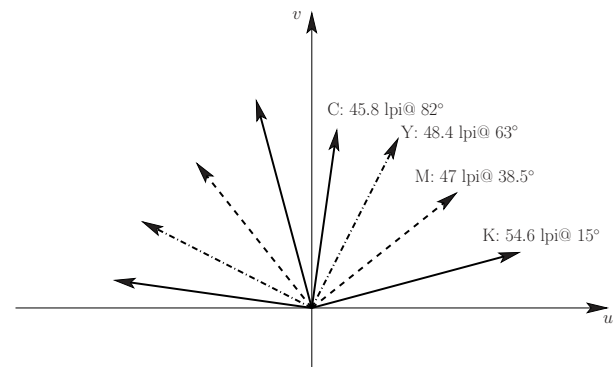
$$T_i(x, y) = \cos\left[2\pi \frac{f_i}{\sqrt{2}}x' + \Psi_i(x, y)\right] \cos\left(2\pi \frac{f_i}{\sqrt{2}}y'\right). \quad (21)$$

Discontinuities in the phase term Ψ_i usually cause undesirable visible artifacts in the halftone separation. The spatial continuity and smoothness of $\Psi_i(x, y)$ is imposed

Table 4 Accuracy for the reflectance-space-based processing and improvement in accuracy for the density-space-based estimation method over the reflectance-space-based estimation for the image set shown in Fig. 20.

Image No.	Accuracy (%) for Reflectance Space Processing				Improvement with Density Space Processing			
	C	M	Y	K	C	M	Y	K
1	95.4	88.4	88.5	95.2	0.1	1.2	1.9	2.6
2	96.5	93.8	95.6	95.0	-0.9	0.3	0.9	4.1
3	95.4	88.0	88.3	94.3	0	0.8	2.3	3.2
4	96.1	91.0	88.8	95.6	-0.4	0.4	0.9	2.5
5	92.7	84.5	84.4	93.7	0.5	1.1	1.7	4.4
6	96.7	90.0	90.3	95.8	-0.3	0.1	1.1	2.3
7	95.5	88.1	88.9	95.0	-0.3	0.3	1.5	2.0
8	95.3	89.4	87.5	94.8	0	0.6	0.8	3.1
9	97.2	92.7	91.7	95.6	-0.2	0.2	-0.2	1.2
10	97.1	91.4	89.9	95.6	-0.5	0	-0.4	1.5
11	94.4	87.0	87.2	94.2	0.3	0.6	0.7	2.7
12	98.5	94.5	95.8	98.4	0	0.4	0.7	0.9
13	94.2	86.2	89.3	94.7	0.4	0.2	1.5	3.4
14	93.9	86.0	86.9	94.6	0.5	0.6	1.5	3.5
15	94.0	88.2	87.0	94.8	0.7	1.5	1.5	3.7
16	95.0	87.2	86.8	94.4	-0.1	0.1	1.3	2.9
17	92.6	83.0	83.3	93.6	0.9	1.5	1.7	4.2
18	92.0	81.9	85.7	92.8	0.4	0.7	2.0	5.2
19	95.9	88.6	89.8	95.4	-0.2	0.2	1.5	1.9
20	96.6	92.0	93.2	97.2	0.3	0.1	0.7	1.9
21	96.2	90.4	90.3	95.9	0.2	0.5	1.4	1.9
22	95.9	88.7	90.1	95.5	0	-0.1	1.2	2.8
23	96.6	89.3	90.9	94.7	-0.6	-0.1	0.9	3.4
24	94.8	87.1	86.5	94.5	-0.1	0.1	1.4	3.6

to minimize these artifacts. The technique is therefore referred to as CPM halftoning. A visual watermark pattern such as a bilevel text image serves as the watermark based on which the phase modulation term Ψ_i for the i 'th halftone separation is determined. Typically, the bilevel watermark is smoothed using a spatial blur to ensure continuity of the phase and the resulting values $w_i(x, y)$ are normalized between $(0, \kappa]$, $\kappa \leq \pi$, to introduce a phase

**Fig. 24** Frequency vectors for stable moire-free C, M, Y, and K halftone screens.

change of κ rad between the two levels of the watermarked image.

The digitally embedded watermark pattern in each separation can be retrieved by overlaying the halftone separation with a corresponding “decoder mask,” which is a halftone image that has the same fundamental screen frequency as the watermarked separation in consideration. It has been analytically demonstrated that the visible pattern after this overlay resembles the embedded watermark pattern, which enables visual detection.²¹ Typically, the decoder mask has 50% area coverage and κ is set to π to enable maximal contrast in the detected watermark.²¹ In our proposed framework, an electronic decoder mask corresponding to the 50% area coverage is used to extract the watermark patterns from the estimates of the individual colorant halftones. The overlay operation is implemented in digital computation by multiplying together “transmittances” of the decoder mask and the estimated halftone, each being set to 0 for colorant-covered regions and 1 otherwise.

5 Experimental Results

Our experimental setup utilized an electrophotographic *CMYK* color printer with an addressability of 600×600 dpi. Stable moiré-free screen frequency configurations are sought to prevent self-detection with CPM (see the details in the appendix for a discussion on self-detection). For this purpose, we used the screen frequencies shown in Fig. 24, which are the scaled versions of the vectors described by Schoppmeyer.⁴⁹ Note that alternatively the methodology developed by Amidror et al.³² can be employed to determine additional stable moiré-free configurations.

In each of the C, M, Y, and K colorant separations, an independent watermark pattern was embedded via CPM. The resulting color halftone was printed on our test printer and scanned with a flatbed *RGB* scanner with an optical resolution of 600×600 dpi. Estimates of the C, M, Y, and K halftones were obtained according to the proposed methodology using the R, G, and B channels of the scanned image. The band-reject filters designed for the frequency vectors shown in Fig. 24 are shown in Fig. 25. The embedded watermark patterns are finally detected by overlaying the estimates with the corresponding decoder masks.

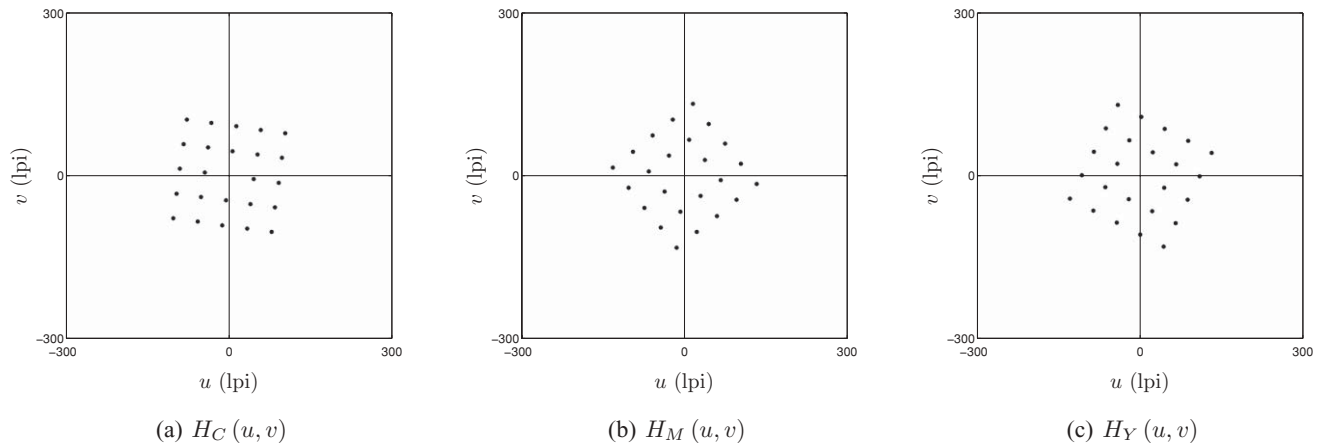


Fig. 25 Narrow-band band-reject filters for eliminating the frequency components of the *CMY* halftone separations from the densities of the *RGB* color channels of the scanned images for the frequency vector configuration shown in Fig. 24. (a) cyan, (b) magenta, and (c) yellow.

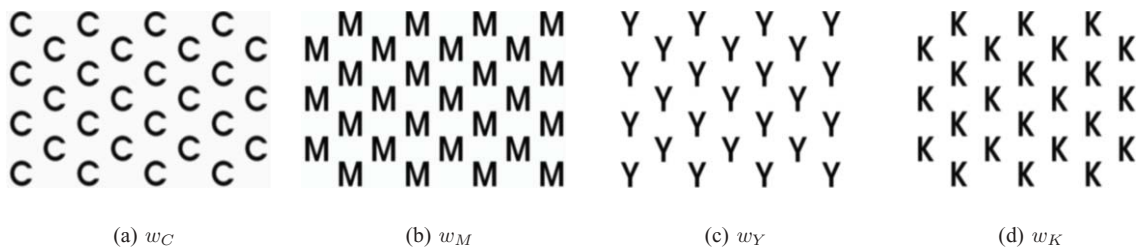


Fig. 26 Watermark patterns for the *C*, *M*, *Y*, and *K* colorant separations. (a) cyan, (b) magenta, (c) yellow, and (d) black.

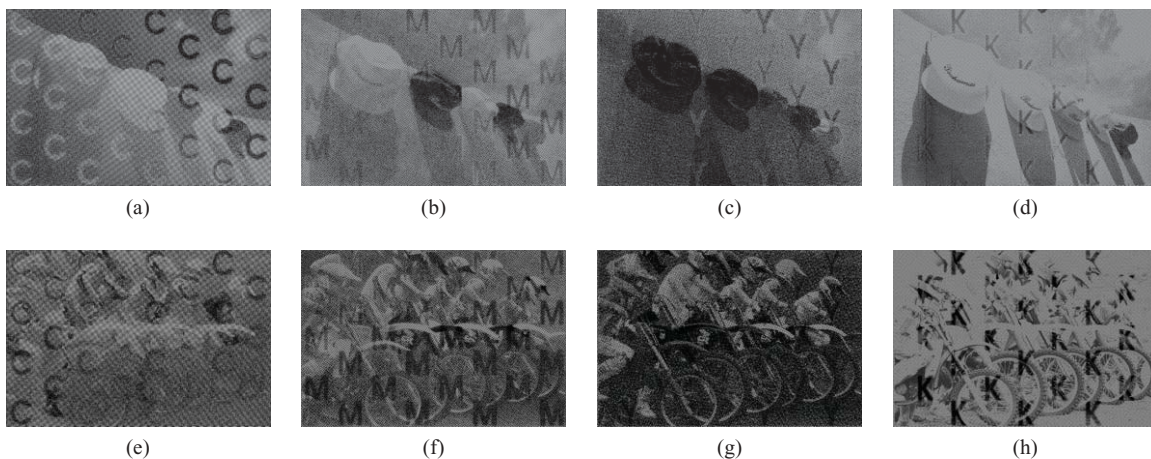


Fig. 27 Detection results on the *CMYK* halftone separation estimates obtained using our methodology: (a) to (d) the detection results for the “Hats” image (e) to (h) the detection results for the “Motorcycles” image. Artifacts due to rescreening in the printing process may not allow clear observation of the detected watermark pattern in the printed version of these figures. Please refer to the electronic version of this paper to clearly observe the detection results. (a) and (e), cyan; (b) and (f), magenta; (c) and (g), yellow; (d) and (h), black.

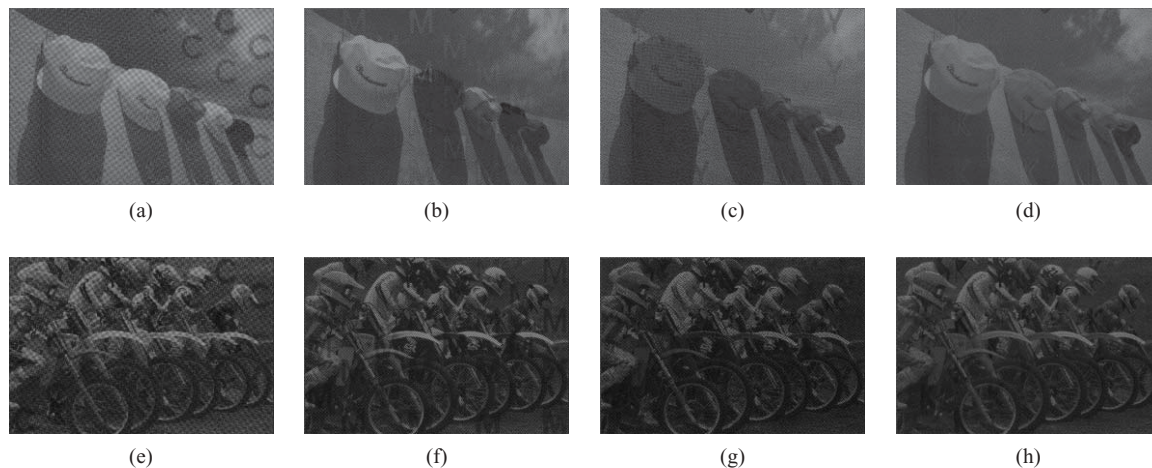


Fig. 28 Detection results on the initial contone scanned *RGB* channel images: (a) to (d) the detection results for the “Hats” image and (e) to (h) the detection results for the “Motorcycles” image. Artifacts due to rescreening in the printing process may not allow clear observation of the detected watermark pattern in the printed version of these figures. Please refer to the electronic version of this paper to clearly observe the detection results. (a) and (e), cyan; (b) and (f), magenta; (c) and (g), yellow; (d) and (h), black.

We illustrate the operation of the proposed methodology using the “Hats” and “Motorcycles” images that are referred to as Image 3 and Image 5 in Fig. 20, respectively. The printed images were generated in 5.12- \times 3.41-in. format and the watermark patterns shown in Fig. 26 were embedded in the corresponding halftone separations. Figure 27 shows the detection results obtained for our example. The watermark patterns are generally visible throughout the images subject to variations due to the content of the corresponding contone image. Specifically, watermarks embedded in the highlights and shadows are harder to detect than the watermarks embedded in the midtones—as is expected from the analysis of *CPM* watermark detection.²¹ This effect is particularly observed in the *Y* and *K* separations. The *Y* separation of the both images includes many dark regions with nearly 100% coverage, and the *K* channel of the “Hats” image includes many bright regions with nearly 0% coverage, which do not allow for meaningful watermark embedding and extraction due to the absence of halftone structure.²¹

For purpose of comparison, we also performed detection using the initial contone scanner channel images that exhibit strong interseparation colorant interactions. Note that the demodulation provided by the electronic decoder mask automatically forms a crude form of spatial filtering in these images because it selectively translates the frequencies corresponding to the mask lattice to low frequencies,²¹ which in fact correspond to the colorant separation of interest, whereas this is not the case for other colorant separations. The watermark patterns embedded in the *C*, *M*, and *Y* halftone separations were detected using the complementary *R*, *G*, and *B* color channels of the scanned images, respectively, and the watermark pattern in the *K* halftone separation was detected using the spectral average of the *RGB* color channels of the scanned images. Figure 28 shows the detection results. We can see that watermarks are visible in some regions where the spectral interference is low, though with rather low contrast. Specifically, it is very hard to detect the watermark pat-

tern embedded in the *K* separation. Comparing Fig. 28 with Fig. 27, we see that our proposed method enables detection of the embedded watermark patterns with much higher contrast.

6 Conclusion

We proposed a methodology for color halftone watermarking that embeds, via a monochrome halftone watermarking method, watermarks in the halftone colorant separations of a clustered-dot color halftone. We demonstrated that by carefully selecting halftone periodicities, the spatial characteristics of the separations and the spectral characteristics of the colorants can be used to estimate the individual *CMYK* halftone separations from scanned *RGB* images, enabling effective detection of the embedded watermarks despite the apparent degeneracy in estimating four colorant halftones from three scanner channels and other undesired colorant interactions. We demonstrated the efficacy of this methodology using *CPM* for the embedding and detection of independent per-separation watermarks—where the proposed method provides much higher watermark contrast at the detector than the alternative of direct detection. The proposed estimation technique can also be used as a general method for estimating *CMYK* halftones from *RGB* scans. For this purpose, we evaluated the accuracy of our estimates in a simulation framework and compared our results against alternative estimation methods. Our evaluations indicate the proposed method provides satisfactory estimation accuracies for the individual *CMYK* halftone separations and performs better than the alternatives.

Appendix: *CPM* Watermark Self-Detection for Singular Halftone Configurations

When the individual separations are subjected to phase modulation for the purpose of watermark embedding, their instantaneous frequencies in different spatial regions vary around a narrow region about their nominal values. For a monochrome halftone with a suitably designed *CPM* watermark, this fre-

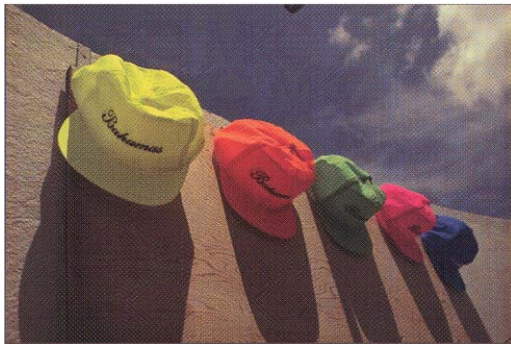


Fig. 29 Self-detectable watermark patterns in a singular moiré-free halftone screen configuration. Artifacts due to rescreening in the printing process may not allow clear observation of the self-detected watermark patterns in the printed version of this figure. Please refer to the electronic version of this paper to clearly observe the self-detectability. (Color online only.)

quency variation is imperceptible.²¹ The overlay of color halftone separations, however, typically exhibits moiré at the sum and difference frequencies of the constituent screen frequencies.³² Therefore, when considering the halftones in overlay, it is also necessary to ensure that the resulting moiré is also imperceptible in the presence of the phase modulation. This requires a careful selection of the set of frequency vectors for the color halftone configuration. If an integer linear combination of the constituent halftone frequency vectors forms a closed polygon, the configuration is referred to as singular.³² For singular configurations, where the integer coefficients resulting in singularity are small (for example, ± 1 or ± 2), the phase modulation causes significant deviations around the dc frequency, visible as objectionable color shifts localized around the modulated regions.^{33,50} These cause an undesired effect that the embedded watermark patterns become visible (without any detection) in the printed color halftone image. We refer to this effect in the singular halftone configurations as watermark self-detection.

Watermark self-detection is specifically observed in the case for the conventional analog 15-, 75-, and 45-deg equifrequency rotated clustered-dot and dot-on/off-dot color halftone geometries. To illustrate self-detection, we employ the set of frequency vectors shown in Fig. 21, which represent a singular moiré-free configuration.³² Using the CPM methodology, we embedded the watermark patterns shown in Fig. 26 in the C, M, Y, and K separations of the *Hats* image. Figure 29 shows a downscaled version of the digital CMYK halftone in which the watermark patterns are visible without any detection.

With this motivation, for color applications of phase-modulation-based halftone embedding, it is preferable to choose configurations that are stable, from a moiré standpoint, against small variations in frequency, as opposed to singular moiré-free geometries.

Acknowledgment

This work was supported in part by an award from the Xerox Foundation and by a grant from New York State Office of Science, Technology & Academic Research (NYSTAR) through the Center for Electronic Imaging Systems (CEIS).

References

1. B. Oztan and G. Sharma, "Clustered-dot color halftone watermarks," in *Proc. IS&T/SID 16th Color Imaging Conf. Color Science and Engineering: Systems, Technologies, Applications*, pp. 99–104, Portland, OR (2008).
2. B. Oztan and G. Sharma, "Clustered-dot color halftone watermarks using spatial frequency and color separability," in *Color Imaging XV: Processing, Hardcopy, and Applications*, R. Eschbach and G. G. Marcu, Eds., *Proc. SPIE* **7528**, 75280Y-1–12 (2010).
3. I. Cox, M. Miller, J. Bloom, J. Fridrich, and T. Kalker, *Digital Watermarking and Steganography*, 2nd ed., Morgan Kaufmann, San Francisco (2007).
4. Special issue on digital watermarking, *IEEE Signal Proc. Mag.* **17** (2000).
5. C. I. Podilchuk and E. J. Delp, "Digital watermarking: algorithms and applications," *IEEE Signal Proc. Mag.* **18**, 33–46 (2001).
6. G. C. Langelaar, I. Setyawan, and R. L. Lagendijk, "Watermarking digital image and video data," *IEEE Signal Proc. Mag.* **17**, 20–46 (2000).
7. R. L. van Renesse, *Optical Document Security*, 3rd ed., Artech House, Boston (2005).
8. I. Amidror, S. Chosson, and R. D. Hersch, "Moiré methods for the protection of documents and products: a short survey," *J. Phys. Conf. Ser.* **77**(1), 012001 (2007).
9. C. M. Briquet, *Les Filigranes: Dictionnaire Histoire Des Marques Due Papier Des Leur Apparition Vers 1282, Jusquen 1600*, 2nd ed., Karl W. Hiersemann, Leipzig (1923).
10. K. T. Knox and S. Wang, "Digital watermarks using stochastic screens," in *Color Imaging: Device Independent Color, Color Hardcopy, and Graphic Arts II*, G. B. Beretta and R. Eschbach, Eds., *Proc. SPIE* **3018**, 316–322 (1997).
11. Z. Baharav and D. Shaked, "Watermarking of dither halftoned images," in *Security and Watermarking of Multimedia Contents*, P. W. Wong and E. J. Delp, Eds., *Proc. SPIE* **3657**, 307–316 (1999).
12. S. Wang and K. T. Knox, "Embedding digital watermarks in halftone screens," in *Security and Watermarking of Multimedia Contents II*, P. W. Wong and E. J. Delp, Eds., *Proc. SPIE* **3971**, 218–227 (2000).
13. H. Z. Hel-Or, "Watermarking and copyright labeling of printed images," *J. Electron. Imaging* **10**, 794–803 (2001).
14. I. Amidror, "New print-based security strategy for the protection of valuable documents and products using moiré intensity profiles," in *Optical Security and Counterfeit Deterrence Technique IV*, R. L. van Renesse, Ed., *Proc. SPIE* **4677**, 89–100 (2002).
15. G. Sharma and S. Wang, "Show-through watermarking of duplex printed documents," in *Security, Steganography, and Watermarking of Multimedia Contents VI*, E. J. Delp and P. W. Wong, Eds., *Proc. SPIE* **5306**, 670–684 (2004).
16. C. Liu, S. Wang, and B. Xu, "Authenticate your digital prints with Glossmark images," in *Proc. IS&T/NIP20: Int. Conf. on Digital Printing Technologies*, pp. 312–316 (2004).
17. S. Huang and J. K. Wu, "Optical watermarking for printed document authentication," *IEEE Trans. Inf. Forens. Secur.* **2**, 164–173 (2007).
18. O. Bulan, V. Monga, G. Sharma, and B. Oztan, "Data embedding in hardcopy images via halftone-dot orientation modulation," in *Security, Forensics, Steganography, and Watermarking of Multimedia Contents X*, E. J. Delp, P. W. Wong, J. Dittmann, and N. D. Memon, Eds., *Proc. SPIE* **6819**, 68190C-1–12 (2008).
19. J.-M. Guo, S.-C. Pei, and H. Lee, "Paired subimage matching watermarking method on ordered dither images and its high-quality progressive coding," *IEEE Trans. Multimed.* **10**, 16–30 (2008).
20. J.-M. Guo and Y.-F. Liu, "Hiding multitone watermarks in halftone images," *IEEE Multimed.* **17**, 34–43 (2010).
21. B. Oztan and G. Sharma, "Continuous phase-modulated halftones," *IEEE Trans. Image Process.* **18**, 2718–2734 (2009).
22. G. Sharma, R. P. Loce, S. J. Harrington, and Y. Zhang, "Illuminant multiplexed imaging: special effects using GCR," in *Proc. IS&T/SID 11th Color Imaging Conf. Color Science and Engineering: Systems, Technologies, and Applications*, pp. 266–271, Scottsdale, AZ (2003).
23. R. L. de Queiroz, K. M. Braun, and R. P. Loce, "Detecting spatially varying gray component replacement with application in watermarking printed images," *J. Electron. Imaging* **14**, 033016, 1–9 (2005).
24. N. Rudaz and R. D. Hersch, "Protecting identity documents by microstructure color differences," *J. Electron. Imaging* **13**, 315–323 (2004).
25. R. D. Hersch, P. Donzé, and S. Chosson, "Color images visible under UV light," *ACM Trans. Graph.* **26**(3), 75.1–75.9 (2007).
26. R. Bala, R. Eschbach, and Y. Zhao, "Substrate fluorescence: bane or boon?" in *Proc. IS&T/SID 15th Color Imaging Conf. Color Science and Engineering: Systems, Technologies, Applications*, pp. 261–266, Albuquerque, NM (2007).
27. C. M. Hains, S. Wang, and K. T. Knox, "Digital color halftones," Chap. 6, in *Digital Color Imaging Handbook*, G. Sharma, Ed., CRC Press, Boca Raton, FL (2003).

28. O. Bulan, V. Monga, and G. Sharma, "High capacity color barcodes using dot orientation and color separability," in *Media Forensics and Security XI*, E. J. D. III, J. Dittmann, N. D. Memon, and P. W. Wong, Eds., *Proc. SPIE* **7254**, 725417-1-7 (2009).
29. J. A. C. Yule, *Principles of Color Reproduction, Applied to Photomechanical Reproduction, Color Photography, and the Ink, Paper, and Other Related Industries*, Wiley, New York (1967).
30. J. W. S. Cassels, *An Introduction to the Geometry of Numbers*, Springer, Berlin (1959).
31. A. Papoulis, *Systems and Transforms with Applications in Optics*, McGraw Hill, New York (1968).
32. I. Amidror, R. D. Hersch, and V. Ostromoukhov, "Spectral analysis and minimization of moiré patterns in color separation," *J. Electron. Imaging* **3**, 295-317 (1994).
33. B. Oztan, G. Sharma, and R. P. Loce, "Misregistration sensitivity in clustered-dot color halftones," *J. Electron. Imaging* **17**, 023004,1-30 (2008).
34. E. Dubois, "The sampling and reconstruction of time-varying imagery with application in video systems," *Proc. IEEE* **73**, 502-522 (1985).
35. D. Kermisch and P. G. Roetling, "Fourier spectrum of halftone images," *J. Opt. Soc. Am.* **65**, 716-723 (1975).
36. T. S. Rao, G. R. Arce, and J. P. Allebach, "Analysis of ordered dither for arbitrary sampling lattices and screen periodicities," *IEEE Trans. Acoust. Speech Signal Proc.* **38**, 1981-2000 (1990).
37. G. Sharma, "Color fundamentals for digital imaging," Chap. 1 in *Digital Color Imaging Handbook*, G. Sharma, Ed., CRC Press, Boca Raton, FL (2003).
38. F. Grum and C. J. Bartleson, Eds., *Optical Radiation Measurements: Color Measurement*, Vol. 2, Academic Press, New York (1980).
39. C. C. MacDuffee, *The Theory of Matrices*, Chelsea, New York (1946).
40. P. Delabastita, "Screening techniques, moiré in four color printing," in *TAGA Proc.*, pp. 44-65 (1992).
41. S. Gustavson, "Color gamut of halftone reproduction," *J. Imaging Sci. Technol.* **41**, 283-290 (1997).
42. J. P. Allebach, "Binary display of images when spot size exceeds step size," *Appl. Opt.* **19**, 2513-2519 (1980).
43. T. N. Pappas and D. L. Neuhoff, "Printer models and error diffusion," *IEEE Trans. Image Process.* **4**, 66-80 (1995).
44. J. P. M. DeSa, *Pattern Recognition: Concepts, Methods, and Applications*, Springer-Verlag, Berlin (2001).
45. P. Heckbert, "Color image quantization for frame buffer display," *Comput. Graph.* **16**, 297-307 (1982).
46. L. Brun and A. Tremeau, "Color quantization," Chap. 9 in *Digital Color Imaging Handbook*, G. Sharma, Ed., CRC Press, Boca Raton, FL (2003).
47. R. J. Pellar and L. D. Green, "Electronic halftone generator," U.S. Patent No. 4149183 (1979).
48. R. J. Pellar, "Electronic halftone generator," U.S. Patent No. 4196451 (1980).
49. J. Schoppmeyer, "Screen systems for multicolor printing," U.S. Patent No. 4537470 (1985).
50. I. Amidror and R. D. Hersch, "Neugebauer and Demichel: dependence and independence in n-screen superpositions for colour printing," *Color Res. Appl.* **25**, 267-277 (2000).



Basak Oztan received his BS degree (with high honors) in electrical and electronics engineering from Middle East Technical University, Ankara, Turkey, in 2003 and his MS and PhD degrees in electrical and computer engineering from the University of Rochester, New York, in 2004 and 2010, respectively. He is currently a postdoctoral research associate with the Department of Computer Science, Rensselaer Polytechnic Institute, Troy, New York. He was a research intern with Xerox Webster Research Center, Webster, New York, during the summers of 2005 and 2006. He is the recipient of a student paper award at 2006 IEEE International Conference on Acoustics, Speech, and Signal Processing (ICASSP) in the image and multidimensional signal processing category. His research interests include color imaging, color halftoning, and multimedia security. Dr. Oztan is a member of SPIE, IS&T, the IEEE, and the IEEE Signal Processing Society. He serves as a reviewer for *IEEE Transactions on Image Processing*, *IEEE Transactions on Information Forensics and Security*, *IEEE Signal Processing Letters*, and the *SPIE/IS&T Journal of Electronic Imaging*.



Gaurav Sharma is an associate professor with the University of Rochester in the department of Electrical and Computer Engineering and in the Department of Bio-statistics and Computational Biology. He is also the director for the Center for Emerging and Innovative Sciences (CEIS), a New York state funded center for promoting joint university-industry research and technology development, housed at the University of Rochester. He received his BE degree in electronics and communication engineering from the Indian Institute of Technology Roorkee (formerly the University of Roorkee) in 1990, his ME degree in electrical communication engineering from the Indian Institute of Science, Bangalore, in 1992, and his MS degree in applied mathematics and his PhD degree in electrical and computer engineering from North Carolina State University, Raleigh, in 1995 and 1996, respectively. From August 1996 through August 2003, he was with Xerox Research and Technology, in Webster, New York, initially as a research staff member and subsequently as a principal scientist. Dr. Sharma's research interests include media security and watermarking, color science and imaging, genomic signal processing, and image processing for visual sensor networks. He is the editor of the *Color Imaging Handbook* (CRC Press, 2003). He is a senior member of the IEEE, a member of Sigma Xi, Phi Kappa Phi, Pi Mu Epsilon, SPIE, IS&T, and the signal processing and communications societies of the IEEE. He was the 2007 chair for the Rochester section of the IEEE and the 2003 chair for the Rochester chapter of the IEEE Signal Processing Society. He currently chairs the IEEE Signal Processing Society's Image Video and Multi-dimensional Signal Processing (IVMSP) technical committee. He is member of the IEEE Signal Processing Society's Information Forensics and Security (IFS) technical committee and an advisory member of the IEEE Standing Committee on Industry DSP. He is an associate editor the *Journal of Electronic Imaging* and was an associate editor for the *IEEE Transactions on Image Processing* and the *IEEE Transactions on Information Forensics and Security*.